Theory of standing spin waves in a finite-size chiral spin soliton lattice

J. Kishine,[1,2] Vl. E. Sinitsyn,[3] I. G. Bostrem,[3] Igor Proskurin,[3,4] F. J. T. Goncalves,[5] Y. Togawa,[5] and A. S. Ovchinnikov[3,6]

[1]*Division of Natural and Environmental Sciences, The Open University of Japan, Chiba 261-8586, Japan*

[2]*Institute for Molecular Science, 38 Nishigo-Naka, Myodaiji, Okazaki 444-8585, Japan*

[3]*Institute of Natural Science, Ural Federal University, Ekaterinburg 620002, Russia*

[4]*Department of Physics and Astronomy, University of Manitoba, Winnipeg, Manitoba, Canada R3T 2N2*

[5]*Department of Physics and Electronics, Osaka Prefecture University, 1-1 Gakuencho, Sakai, Osaka 599-8531, Japan*

[6]*Institute of Metal Physics, Ural Division, Russian Academy of Sciences, Ekaterinburg 620219, Russia*

(Received 25 March 2019; revised manuscript received 11 June 2019; published 9 July 2019)

We present a theory of standing spin waves (SSW) in a monoaxial chiral helimagnet. Motivated by experimental findings on the magnetic-field dependence of the resonance frequency in thin films of $CrNb_3S_6$ [Goncalves *et al.*, Phys. Rev. B **95**, 104415 (2017)], we examine the SSW over a chiral soliton lattice (CSL) excited by an ac magnetic field applied parallel and perpendicular to the chiral axis. For this purpose, we generalize Kittel-Pincus theories of the SSW in ferromagnetic thin films to the case of a noncollinear helimagnet with the surface end spins, which are softly pinned by an anisotropy field. Consequently, we found that there appear two types of modes. One is a Pincus mode that is composed of a long-period Bloch wave and a short-period ripple originated from the periodic structure of the CSL. Another is a short-period Kittel ripple excited by space-periodic perturbation, which exists only in the case in which the ac field is applied perpendicular the chiral axis. We demonstrate that the existence of the Pincus mode and the Kittel ripple is consistent with the experimentally found double resonance profile.

DOI: 10.1103/PhysRevB.100.024411

I. INTRODUCTION

Dynamical responses to external probes disclose the nature of collective excitations in condensed matter. Thin ferromagnetic films in this regard have received much attention in recent years due to striking features never seen in bulk samples, and they have been widely applied to technology [1].

At the same time, recent studies of thin films and micrometer-sized crystals of the monoaxial chiral helimagnet $CrNb_3S_6$ have exhibited a number of remarkable phenomena, thereby making this system highly attractive for spintronic applications. These include detection of the chiral spin soliton lattice (CSL) by using Lorenz microscopy and small-angle electron diffraction [2], a sequence of jumps in magnetoresistance [3,4], and magnetic soliton confinement [5,6]. It was argued that the discretization effects result from a specific domain structure, 1-μm-wide grains with different crystallographic structural chirality. In this system, the direction of in-plane magnetic moments is pinned down around the domain boundary.

An obvious consequence of the pinning effect other than quantization of magnetization and magnetoresistance is the emergence of the intrinsic resonance frequency [7]. The early studies on spin resonance in monoaxial chiral helimagnets relied on a spin-wave spectrum of an infinite system and completely ignored this circumstance [8,9]. A recent report on magnetic resonance in microsized crystals $CrNb_3S_6$ revealed that the dynamical resonances of the CSL are sensitive to the polarization of the driving microwave field [10]. In the case in which the microwave field is applied parallel to the chiral axis, the resonance profile was attributed to excitation of standing spin waves (SSWs) [11]. On the other hand, when the microwave field is applied perpendicular to the chiral axis, two resonance modes, with the frequency difference being a few GHz, appear across the entire CSL phase. Furthermore, the resonance modes become asymmetric with regard to the directions of a static field applied perpendicular to the chiral axis to stabilize the CSL. The origins of these two prominent features, namely (i) double resonance and (ii) asymmetry, have not been known as yet. This situation motivates us to elaborate a possible mechanism of these phenomena based on standing spin-wave excitations, which was equally valid both for the parallel and perpendicular microwave fields.

For this purpose, we start by turning our attention to the theory of ferromagnetic resonance (FMR) in thin films, pioneered by Kittel [12]. In Kittel's theory, the surface spins are essentially pinned down by a strong surface anisotropy field. The case of soft pinning was later considered by Pincus [13]. In the case of soft pinning, the eigenfrequencies of the interior spin wave are required to match the Larmor frequency of the surface spins. This matching condition is given by the Davis-Puszkarski equation [14–16], which leads to allowed values of the wave vector of the spin-wave modes.

Since the first observation in permalloy films [17], the detection of the SSW has long attracted considerable attention, including manganite films [18], magnonic crystals [19], and ferromagnetic bars [20]. The SSW has also been regarded as a candidate for working media in spintronics, including Co multilayers [21], a ferrite film [22,23], and spin-torque excitation in YIG/Co heterostructures [24]. Detection of the SSW by FMR is also used to probe the interface exchange-biased structure [25].

However, so far little attention has been paid to the SSW in a magnetic system with a noncollinear ground state, simply because of a lack of experimental motivation. In this regard, we expect that clarifying the nature of the SSW in a chiral helimagnetic system may open a new window to the field. In particular, a purpose of this paper is to reproduce the magnetic resonance profile in microsized $CrNb_3S_6$ [10], with the aid of a theory of SSW over the CSL. We provide evidence that the chiral soliton lattice allows two types of standing waves, either with "soft" (Pincus) or with "hard" (Kittel) pinning of the boundary spins. The ac field applied parallel to the chiral axis excites only standing waves of Pincus type, while being oriented perpendicular to the chiral axis gives rise to a superposition of the Pincus and Kittel modes.

This paper is organized as follows. In Sec. II, we describe a model. In Sec. III, we present results of numerical simulations of SSWs based on equations of motion for the spins. In Sec. IV, we present a detailed analytical theory based on the generalized Davis-Puszkarski scheme. The discussions and conclusions are given in Sec. V.

II. MODEL

In this section, we present a model to describe the SSW in a monoaxial chiral helimagnet. What is essential is a correct description of the ground state of a finite-size soliton lattice with surface spins at the boundaries of a domain with a definite chirality. In this respect, we note that in most of the previous theoretical studies [6] the linear size of the system is assumed to be infinite, though some confinement effects in a finite-size system have been proposed [26,27].

The pinning effects are implemented through surface anisotropy described by two equivalent manners. The atomic discrete lattice approach was used in Refs. [13,28] as opposed to the continuum model developed by Rado and Weertman [29,30]. We will follow the former approach below. Before going into detail, we would like to emphasize that the studies [13,28] resort to a trick to convert the phenomenological expression for magnetocrystalline anisotropy into a vector of the so-called anisotropy field. This effective field is very useful to study spin dynamics based on the Landau-Lifshitz-Gilbert equation, however it assumes time-reversal symmetry breaking (see Ref. [31] for details).

$CrNb_3S_6$ crystal has localized spins $S = 3/2$ carried by Cr^{3+} ions and the strong intralayer ferromagnetic coupling strength, $J_\perp \sim 154$ K, although the weak interlayer ferromagnetic coupling strength is $J \sim 18$ K and the weaker DM interaction strength is $D \sim 2.9$ K [32]. This layered structure with strong intralayer ferromagnetic correlation makes it legitimate to describe the system based on an effective one-dimensional classical Hamiltonian,

$$H = -J\sum_{\langle i,j\rangle} \boldsymbol{S}_i \cdot \boldsymbol{S}_j - \boldsymbol{D}\cdot\sum_{\langle i,j\rangle} \boldsymbol{S}_i \times \boldsymbol{S}_j - [\boldsymbol{H}_0 + \boldsymbol{h}(t)]\cdot\sum_i \boldsymbol{S}_i - \sum_{\sigma=\mathrm{l,r}} \boldsymbol{H}_s \cdot \boldsymbol{S}_\sigma, \quad (1)$$

where $\boldsymbol{S}_i$ is the local spin vector located at the site i, $J > 0$ is the nearest-neighbor ferromagnetic exchange interaction, and $\boldsymbol{D} = D\hat{\mathbf{e}}_z$ is the monoaxial DM interaction vector along a certain crystallographic chiral axis (taken as the z-axis). We take the z-axis as the monochiral-axis and let the linear size be L. Both ends are specified by $z = \pm L/2$. $\boldsymbol{H}_0 = H_0\hat{\mathbf{e}}_x$ is the external magnetic dc field and $\boldsymbol{h}(t)$ is a microwave ac field, given in units of $g\mu_B$. The first two sums are restricted to the nearest neighbors, and the sum over s is a sum over the spins on the left ($\sigma = \mathrm{l}$) and right ($\sigma = \mathrm{r}$) boundary surfaces. As experimentally indicated [5], the constant surface anisotropy field $\boldsymbol{H}_s = H_s\hat{\mathbf{e}}_x$ is assumed to lie in the plane of the film (xz-plane), i.e., $\boldsymbol{H}_s$ is parallel to the uniform dc field $\boldsymbol{H}_0$. Because of the soft boundary condition that originated from $\boldsymbol{H}_s$, the end surface spins $\boldsymbol{S}_\mathrm{l}$ and $\boldsymbol{S}_\mathrm{r}$ have their own dynamics distinguished from the interior spins $\boldsymbol{S}_i$, as schematically indicated in Fig. 1(a).

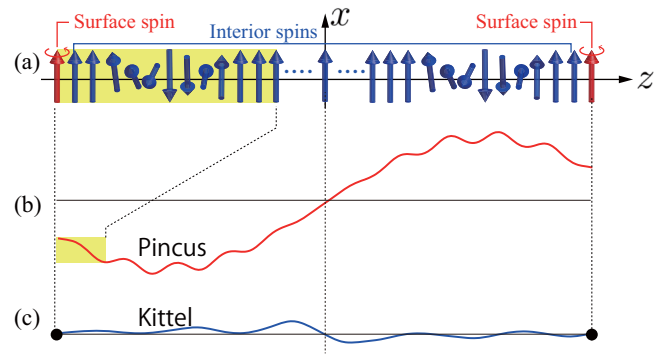

FIG. 1. (a) The interior (blue) and surface end (red) spins that form the chiral soliton lattice. (b) The soft boundary condition gives rise to the Pincus mode, which is incommensurate with respect to the background system. (c) The perpendicular ac field $\beta_x(\tau)$ further excites the additional Kittel mode (ripple), which is pinned down at both ends and commensurate with respect to the background system.

Now, we separately treat the dynamics of the interior and end spins. To analyze the dynamics of the interior spins, the term with $\boldsymbol{H}_s$ can be discarded. Long period modulation of the magnetic structure makes it legitimate to take a continuum limit of the lattice Hamiltonian (1),

$$\mathcal{H}_{\mathrm{interior}} = \frac{JS^2}{2}(\partial_z\theta)^2 + \frac{JS^2}{2}\sin^2\theta(\partial_z\varphi)^2 - DS^2\sin^2\theta\,\partial_z\varphi - [H_0 + h_x(t)]S\sin\theta\cos\varphi - h_z(t)S\cos\theta. \quad (2)$$

Here, φ and θ are the angles that the magnetization, $\boldsymbol{S}(\mathbf{r}) = S(\sin\theta\cos\varphi, \sin\theta\sin\varphi, \cos\theta)$, makes with respect to the x and z axis, respectively, with the film lying parallel to the xz plane. The field $\boldsymbol{H}_0$ is directed along the x-axis. The presence of the field alters a helical spin arrangement of the ground state to the chiral soliton lattice [6,33]. The classical equations of motion, $\hbar S\sin\theta\,\partial_t\theta = \delta\mathcal{H}_{\mathrm{interior}}/\delta\varphi$ and $\hbar S\sin\theta\,\partial_t\varphi = -\delta\mathcal{H}_{\mathrm{interior}}/\delta\theta$, can be easily shown to be

$$\partial_\tau\theta = -\sin\theta\,\partial_z^2\varphi - 2\cos\theta\,\partial_z\theta\,\partial_z\varphi + 2(D/J)\cos\theta\,\partial_z\theta + [\beta_0 + \beta_x(t)]\sin\varphi, \quad (3)$$

$$-\sin\theta\,\partial_\tau\varphi = \sin\theta\cos\theta(\partial_z\varphi)^2 - \partial_z^2\theta - 2(D/J)\sin\theta\cos\theta\,\partial_z\varphi - [\beta_0 + \beta_x(t)]\cos\theta\cos\varphi + \beta_z(t)\sin\theta, \quad (4)$$

where $\tau = JSt/\hbar$, $\beta_0 = H_0/JS$, and $\beta_{x,z}(t) = h_{x,z}(t)/JS$. We note that the frequency scale is $JS/\hbar \sim 3.5 \times 10^{12}$ Hz (by choosing $J = 18$ K [32] and $S = 3/2$).

The ground state is specified by $\theta_0 = \pi/2$ and

$$\varphi_0(z) = \phi_0 - 2\mathrm{am}\left(\frac{\sqrt{\beta_0}}{\kappa} z + \phi_1\right). \tag{5}$$

Here, am is the Jacobi amplitude function. The elliptic modulus κ and two constants, ϕ_0 (0 or π) and ϕ_1 (0 or K), are chosen through fitting with the numerical data (see Sec. III). The spatial period of the CSL is $L_{\mathrm{CSL}} = 2\kappa K/\sqrt{\beta_0}$ and the total number of solitons is $n = L/L_{\mathrm{CSL}}$ [34]. Here, K is the elliptic integral of the first kind.

To consider small dynamical fluctuations around the equilibrium configuration of the CSL, we introduce the $\psi(z,t)$ (out-of-plane) and $\chi(z,t)$ (in-plane) fluctuations of the local spins,

$$\begin{aligned} \theta(z,\tau) &= \frac{\pi}{2} + \psi(z,\tau), \\ \varphi(z,\tau) &= \varphi_0(z) + \chi(z,\tau), \end{aligned} \tag{6}$$

where $|\psi|, |\chi| \ll 1$. Then, a linear approximation of Eqs. (3) and (4) leads to (see Appendix A)

$$\frac{\kappa^2}{\beta_0}\frac{\partial\psi(z,t)}{\partial\tau} = \hat{\mathcal{L}}_\varphi \chi(z,t) + \frac{\kappa^2}{\beta_0}\beta_x(\tau)\sin\varphi_0(z), \tag{7}$$

$$\frac{\kappa^2}{\beta_0}\frac{\partial\chi(z,t)}{\partial\tau} = -\hat{\mathcal{L}}_\theta \psi(z,t) - \frac{\kappa^2}{\beta_0}\beta_z(\tau), \tag{8}$$

where $\hat{\mathcal{L}}_\varphi = -\partial_{\bar{z}}^2 + 2\kappa^2\mathrm{sn}^2\bar{z} - \kappa^2$ and $\hat{\mathcal{L}}_\theta = -\partial_{\bar{z}}^2 + 2\kappa^2\mathrm{sn}^2\bar{z} + 4 - 3\kappa^2$ are the linear Lamé operators, and $\bar{z} = z\sqrt{\beta_0}/\kappa$, with sn being the Jacobi sn function. Due to the presence of the perpendicular ac field, β_x, these equations differ slightly from those used in Ref. [35] to describe coherent sliding motion of the CSL when a time-dependent ac field is applied parallel to the chiral axis.

We comment here on the structure of the EOMs. $\hat{\mathcal{L}}_\varphi$ and $\hat{\mathcal{L}}_\theta$ give the propagating wave described by the eigenfunctions of the Lamé equation. The propagating solution gives the spin resonance in an infinite system [8]. In the present case, the soft boundary condition gives rise to standing waves, where the end surface spins softly fluctuate. We call this mode the "Pincus mode" [see Fig. 1(b)], which is incommensurate with respect to the background system.

Next, the dynamics of the surface spins is described by (see Appendix B for details)

$$\begin{aligned} \frac{\partial\psi_s}{\partial\tau} &= \pm\partial_z\chi_s - \frac{1}{2}\partial_z^2\chi_s \mp (D/J)\partial_z\varphi_0\partial_z\chi_s \\ &\quad + \beta_x(\tau)\sin\varphi_0 + (\beta_s + \beta_0)\cos\varphi_0\chi_s, \end{aligned} \tag{9}$$

$$\begin{aligned} \frac{\partial\chi_s}{\partial\tau} &= \mp\partial_z\psi_s + \frac{1}{2}\partial_z^2\psi_s + \frac{1}{2}(\partial_z\varphi_0)^2\psi_s \\ &\quad + (D/J)(\partial_z\varphi_0)\psi_s - \frac{1}{2}(D/J)\left(\partial_z^2\varphi_0\right)\psi_s \\ &\quad - \{[\beta_s + \beta_0 + \beta_x(\tau)]\cos\varphi_0\}\psi_s, \end{aligned} \tag{10}$$

where $\beta_s = H_s/JS$ is the pinning field strength. The upper (lower) sign refers to the end spins at the right (left) end site, $z = L/2$ or $-L/2$, that are indexed by $s = r$ or l, respectively.

The precession of the surface spins with the frequency, $\Omega_{\mathrm{surface}}$, is eventually caught up in the interior spin wave with the frequency, $\Omega_{\mathrm{interior}}$. Then, the matching condition $\Omega_{\mathrm{surface}} = \Omega_{\mathrm{interior}}$, which is called the Davis-Puszkarski equation [14–16], determines the overall spin-wave dispersion. The SSW modes are quite sensitive to the direction of the external magnetic $\boldsymbol{h}(t)$, i.e., whether $\boldsymbol{h}(t)$ is parallel to the chiral axis [$\boldsymbol{h}(t) = h_{0z}\hat{\mathbf{e}}_z$] or perpendicular to the chiral axis [$\boldsymbol{h}(t) = h_{0x}\hat{\mathbf{e}}_x$].

Before presenting the detailed analysis, we give an intuitive argument on this effect. In Eq. (7), the term including $\beta_x(\tau)\sin\varphi_0(z)$ plays a role of space-time-dependent external force whose "spatial frequency" is equal to the spatial period of the CSL, L_{CSL}. Therefore, when $\beta_x(\tau)$ is present, there appears a series of the additional standing spin waves with their basis spanned by the eigenfunctions of the Lamé equation. These additional modes are completely pinned down at both ends, $z = \pm L/2$. We call this mode "Kittel ripple" [see Fig. 1(c)], which appears only for finite $\beta_x(\tau)$ and commensurate to the background system. Unlike the case of $\beta_x(\tau)$, the term including $\beta_z(\tau)$ in Eq. (8) is spatially uniform and can excite the Pincus mode only. As we will discuss in more detail below, the presence or absence of the Kittel ripple may provide an explanation for the experimentally found difference in the SSW modes depending on the direction of the ac field [10].

III. NUMERICAL SIMULATIONS

A. Simulation scheme

To gain insight into the resonant dynamics, we first perform numerical simulations similar to those used to study CSL sliding motion driven by a parallel magnetic ac field [35]. The numerical analysis is based on the lattice version of Eqs. (3) and (4) for the interior spins,

$$\begin{aligned} \frac{\partial\theta_i}{\partial\tau} &= \sqrt{1 + (D/J)^2}\sin\theta_{i-1}\sin(\varphi_i - \varphi_{i-1} - \delta) \\ &\quad - \sqrt{1 + (D/J)^2}\sin\theta_{i+1}\sin(\varphi_{i+1} - \varphi_i - \delta) \\ &\quad + [\beta_0 + \beta_x(\tau)]\sin\varphi_i, \end{aligned} \tag{11}$$

$$\begin{aligned} \frac{\partial\varphi_i}{\partial\tau} &= -(\cos\theta_{i+1} + \cos\theta_{i-1}) \\ &\quad + \sqrt{1 + (D/J)^2}\cot\theta_i\sin\theta_{i-1}\cos(\varphi_i - \varphi_{i-1} - \delta) \\ &\quad + \sqrt{1 + (D/J)^2}\cot\theta_i\sin\theta_{i+1}\cos(\varphi_{i+1} - \varphi_i - \delta) \\ &\quad + [\beta_0 + \beta_x(\tau)]\cot\theta_i\cos\varphi_i - \beta_z(\tau), \end{aligned} \tag{12}$$

where $\delta = \arctan(D/J)$, and complemented by equations for the boundaries (B2) and (B3). For the boundary spins, β_x is substituted for $\beta_s + \beta_x$. The length of the system is chosen as $L = 411$, which corresponds to the number of kinks accommodated inside the system, $n_{\max} = [Lq_s/2\pi] = 10$. The value is about the same order of magnitude as the number of kinks confined within grains of a definite crystalline chirality in thin films of $CrNb_3S_6$ [2], where the pitch of the helix is $q_s = 0.16$.

A search for a static configuration of the ground state is described in detail in Ref. [35]. The static solution found with the aid of the relaxation method serves as an initial condition

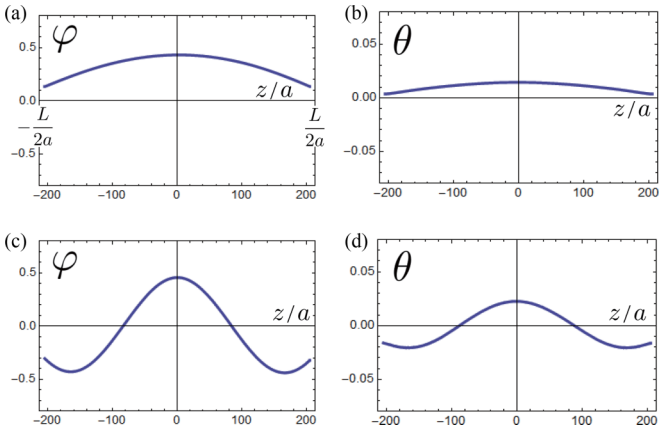

FIG. 2. The spatial profiles of φ and θ associated with the standing waves over the helical structure under zero dc magnetic field ($\beta_0 = 0$). The ac field is applied parallel to the chiral axis. The SSW of the first order at the frequency $\Omega = 0.0011$ (a,b) and of the third order at the frequency $\Omega = 0.0030$ (c,d). The parameters are taken as $\beta_s = 0.02$ and $\beta_{z0} = 0.0001$.

for the dynamical equations addressed by the eighth-order Dormand-Prince method with an adaptive step-size control. To search for a resonant frequency, the following procedure is adopted. Time evolution of $\varphi_i(\tau)$, $\theta_i(\tau)$ is determined as a response to the ac field $\beta_\alpha(\tau) = \beta_{\alpha 0}[1 - \exp(-\tau)]$ ($\alpha = x, z$) at the start. The Fourier transform of the ac-field signal is distributed over a continuous frequency range that enables us to localize an approximate position of an intrinsic resonance. To get its precise value, the spin dynamics equations are again integrated but now the ac field is periodic, $\beta_\alpha(\tau) = \beta_{\alpha 0} \sin(\Omega\tau)$, where $\alpha = x$ or z. Provided that the frequency Ω lies near the resonance, this gives rise to characteristic beatings. Reexamination of these signals by Fourier analysis specifies an exact position of the resonance frequency.

Here, we separately discuss the results of numerical solution for configurations examined experimentally in Ref. [10]: when (I) the ac microwave field is applied parallel to the chiral axis, and when (II) the ac field is applied perpendicular to the axis.

B. Case I: The ac magnetic field is parallel to the chiral axis

In case I, we expect the driving ac field to excite the Pincus modes, which are symmetric with respect to reflection across the center ($z = 0$), because the pinning fields $\beta_s(t)$ act on both ends in a symmetric manner.

In Fig. 2, we show the spatial profiles of φ and θ associated with the standing waves over the helical structure under a zero dc magnetic field ($\beta_0 = 0$). The parameters are taken as $\beta_s = 0.02$ and $\beta_{z0} = 0.0001$. The SSWs of the first and third orders occur at the frequencies $\Omega = 0.0011$ and 0.0030, respectively. As is evident from Fig. 2, there arise SSWs with the number of half-wavelengths being approximately odd in a similar way to those in the original Kittel theory [12]. It should be noted that the amplitude of the φ-oscillations is ten times the θ-mode amplitude. These findings fit into the idea that spin-wave modes in a thin film behave like a vibration of a rope clamped at both ends, when some anisotropy field essentially or partially pins down boundary spins.

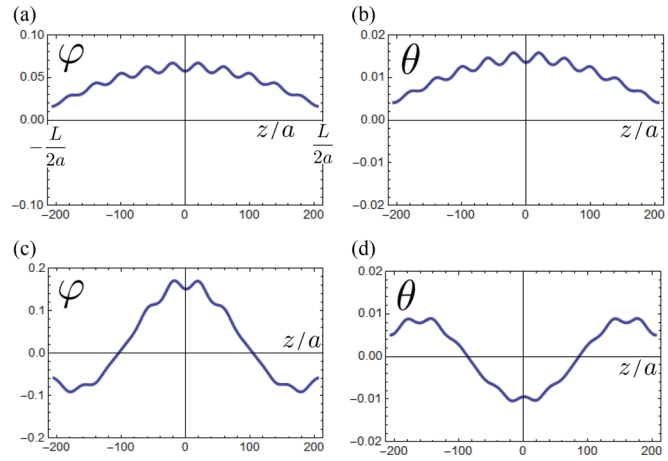

FIG. 3. The spatial profiles of φ and θ associated with the standing waves over the CSL structure under finite dc magnetic field ($\beta_0 = 0.002$). The ac field is applied parallel to the chiral axis. The SSW of the first order at the frequency $\Omega = 0.001\,05$ (a,b), and of the third order at the frequency $\Omega = 0.003\,05$ (c,d). The parameters are taken as $\beta_s = 0.02$ and $\beta_{x0} = 0.0001$.

In Fig. 3, we show the spatial profiles of φ and θ associated with the standing waves over the CSL structure under a finite dc magnetic field ($\beta_0 = 0.002$). The parameters are taken as $\beta_s = 0.02$ and $\beta_{x0} = 0.0001$. The SSWs of the first and third orders occur at the frequencies $\Omega = 0.001\,05$ and $0.003\,05$, respectively. Just as in the case of Fig. 2, one may immediately recognize the symmetric modes with zero and two nodes, but the profiles of these excitations look different. It is clear that some short-scale oscillations, seen as a ripple over the standing wave background, contribute to the signal. We will discuss the origin of this ripple in Sec. IV.

C. Case II: The ac magnetic field is perpendicular to the chiral axis

Next we consider case II. In this case, we expect the driving ac field to excite the Pincus modes, which are antisymmetric with respect to reflection across the center ($z = 0$), because in Eq. (7) the space-dependent field $\sin\varphi_0(z)$ is an odd function of z.

In Fig. 4, we show the spatial profiles of φ and θ associated with the standing waves over the helical structure under a zero dc magnetic field ($\beta_0 = 0$). The parameters are taken as $\beta_s = 0.02$ and $\beta_{x0} = 0.0001$. The SSW of the second order

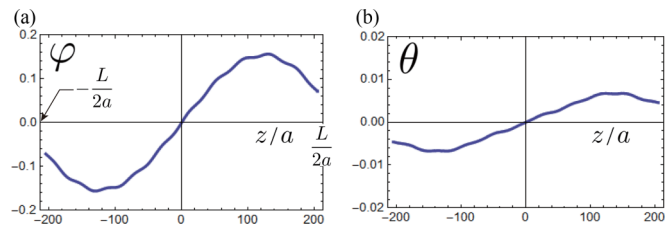

FIG. 4. The spatial profiles of (a) φ and (b) θ associated with the second-order standing waves over the helical structure under zero dc magnetic field ($\beta_0 = 0$). The ac field is applied perpendicular to the chiral axis at the frequency $\Omega = 0.0021$.

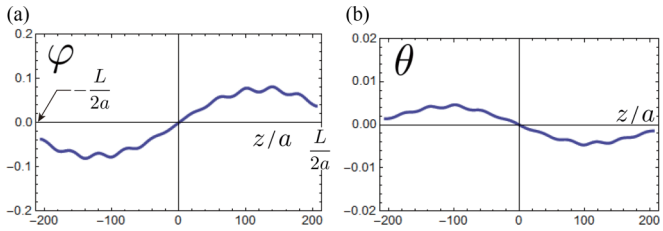

FIG. 5. The spatial profiles of (a) φ and (b) θ associated with the second-order standing waves over the CSL structure under finite dc magnetic field ($\beta_0 = 0.002$). The ac field is applied perpendicular to the chiral axis at the frequency $\Omega = 0.0022$.

occurs at the frequencies $\Omega = 0.0021$. As compared with case I, shown in Fig. 2, we recognize that the additional ripples with a tiny amplitude are superimposed on the background Pincus mode. These additional ripples are caused by the space-time-dependent external force, $\beta_x(\tau)\sin\varphi_0(z)$. Because the term $\sin\varphi_0(z)$ vanishes at both ends $z = \pm L/2$, the additional modes are analogous to the original Kittel modes [12], which are completely pinned down at both ends.

In Fig. 5, we show the spatial profiles of φ and θ associated with the standing waves over the CSL structure under a finite dc magnetic field ($\beta_0 = 0.002$). The parameters are taken as $\beta_s = 0.02$ and $\beta_{x0} = 0.0001$. The SSW of the second order occurs at the frequencies $\Omega = 0.0022$. As with the case shown in Fig. 4, the additional Kittel ripples are superimposed on the background Pincus mode, although it is almost invisible because of tiny amplitudes.

Based on the numerical findings presented above, it is evident that the SSW modes are significantly affected by the movable boundaries, which causes Pincus modes. Furthermore, when the ac field is applied perpendicular to the chiral axis (case II), the additional Kittel ripples are superimposed. Our next challenge is to elaborate an appropriate analytical theory of the dynamics.

IV. ANALYTICAL THEORY OF THE SSW DYNAMICS

In this section, we present an analytical theory in detail. We consider the following four cases depending on "case I or II" and "the SSW over either CSL or helical structure." Throughout this section, we follow the technical scheme for the Davis-Puszkarski equation, which is summarized in Appendix C from general viewpoints.

A. Case I: The ac magnetic field is parallel to the chiral axis

1. SSW over the CSL

In case I, the interior spins are subject to the uniform ac field only. In Eqs. (7) and (8), $\beta_x(\tau) = 0$ and only the spatially uniform field, $\beta_z(\tau)$, excites the intrinsic SSW modes. So, we can also drop $\beta_z(\tau)$ for the purpose of obtaining the SSW dispersion. Then, the coupled equations are solved by separation of variables, $\chi(z,\tau) = \nu(\bar{z})Z(\tau)$ and $\psi(z,\tau) = \nu(\bar{z})\xi(\tau)$. Both χ and ψ fields share the same spatial parts $\nu(\bar{z})$, which is the eigenfunction of the Lamé equation [6,36], and satisfy

$$\hat{\mathcal{L}}_\varphi \nu_q(\bar{z}) = \lambda^{(\varphi)}\nu_q(\bar{z}) = \kappa'^2 \mathrm{sn}^2(\alpha,\kappa')\nu_q(\bar{z}), \tag{13}$$

$$\hat{\mathcal{L}}_\theta \nu_q(\bar{z}) = \lambda^{(\theta)}\nu_q(\bar{z}) = [\kappa'^2 \mathrm{sn}^2(\alpha,\kappa') + 2 + 2\kappa'^2]\nu_q(\bar{z}). \tag{14}$$

Here, the real parameter α lies in the range $-K' < \alpha < K'$, where K' is the elliptic integral of the first kind with the complementary elliptic modulus, $\kappa'^2 = 1 - \kappa^2$. The lower index of the eigenfunctions stands for the wave number of the Bloch wave,

$$q(\alpha) = \frac{\sqrt{\beta_0}}{\kappa}\left[Z(\alpha,\kappa') + \frac{\pi\alpha}{2KK'}\right], \tag{15}$$

which is related with the eigenvalues $\lambda^{(\varphi,\theta)}$ through an implicit parameter α [37]. $Z(\alpha,\kappa')$ represents Jacobi's zeta-function. The allowed values of $q(\alpha)$ are to be determined by this equation.

The temporal parts $Z(\tau)$ and $\xi(\tau)$ are merely the collective coordinates associate with φ and θ fields, respectively, and describe the collective dynamics of the CSL as a whole. Then, Eqs. (7) and (8) become

$$\dot{\xi}(\tau) = C_1\left(\frac{\beta_0}{\kappa^2}\right)Z(\tau), \qquad \dot{Z}(\tau) = -C_2\left(\frac{\beta_0}{\kappa^2}\right)\xi(\tau), \tag{16}$$

and we immediately have the eigenfrequency $\Omega_0 = (\beta_0/\kappa^2)\sqrt{C_1C_2}$ that contains the arbitrary constants $C_{1,2}$, which characterize the separation of variables $[(\kappa^2/\beta_0)[Z(\tau)]^{-1}\partial\xi(\tau)/\partial\tau = [\nu(\bar{z})]^{-1}\hat{\mathcal{L}}_\varphi\nu(\bar{z}) = C_1$, for example].

Using (13) and (14), we have $C_1C_2 = \lambda^{(\varphi)}\lambda^{(\theta)}$, which gives rise to the resonance frequency for the interior SSW,

$$\Omega^2_{\mathrm{interior}}(q) = \frac{\beta_0^2}{\kappa^4}\kappa'^2\mathrm{sn}^2(\alpha,\kappa')[\kappa'^2\mathrm{sn}^2(\alpha,\kappa') + 2 + 2\kappa'^2]. \tag{17}$$

Then, we use the symmetrical solution of the Lamé equation [6,36,37],

$$\nu_q(\bar{z}) \propto \mathrm{Re}\left[\frac{\theta_4\left(\frac{\pi}{2K}[\bar{z} - i\alpha - K]\right)}{\theta_4\left(\frac{\pi\bar{z}}{2K}\right)}e^{-i\bar{q}\bar{z}}\right], \tag{18}$$

where $\bar{z} = \sqrt{\beta_0}/\kappa(z - L/2) + K$, and θ_4 is the Jacobi theta function.

Next, we solve the equations of motion for the end surface spins, Eqs. (9) and (10), by means of a separation of variables, $\chi_{r,l}(z,\tau) = \nu_q(z)Z_s(\tau)$, $\psi_{r,l}(z,\tau) = \nu_q(z)\xi_s(\tau)$. Here, $\bar{q} = (\kappa/\sqrt{\beta_0})q(\alpha)$. It should be noted that the spatial part $\nu_q(z)$ is the same as that for the interior spins. This trick, used throughout this paper, provides the resonance frequency for

the end surface spins [11],

$$\Omega^2_{\rm surface} = \frac{1}{\nu_q^2(\bar{z}_{L/2})}\left[\frac{\sqrt{\beta_0}}{\kappa}\nu_q'(\bar{z}_{L/2}) - \frac{\beta_0}{2\kappa^2}\nu_q''(\bar{z}_{L/2}) - \frac{D}{J}\frac{\beta_0}{\kappa^2}\varphi_0'(\bar{z}_{L/2})\nu_q'(\bar{z}_{L/2}) + (\beta_0+\beta_s)\cos\varphi_0(\bar{z}_{L/2})\nu_q(\bar{z}_{L/2})\right]$$
$$\times\left[\frac{\sqrt{\beta_0}}{\kappa}\nu_q'(\bar{z}_{L/2}) - \frac{\beta_0}{2\kappa^2}\nu_q''(\bar{z}_{L/2}) - \frac{\beta_0}{2\kappa^2}\nu_q(\bar{z}_{L/2})(\varphi_0')^2(\bar{z}_{L/2}) - \frac{D}{J}\left\{\frac{\sqrt{\beta_0}}{\kappa}\varphi_0'(\bar{z}_{L/2}) - \frac{\beta_0}{2\kappa^2}\varphi_0''(\bar{z}_{L/2})\right\}\nu_q(\bar{z}_{L/2})\right.$$
$$\left. + (\beta_0+\beta_{\rm s})\cos\varphi_0(\bar{z}_{L/2})\nu_q(\bar{z}_{L/2})\right]. \tag{19}$$

Now, the matching condition (the Davis-Puszkarski equation)

$$\Omega_{\rm interior}(q) = \Omega_{\rm surface} \tag{20}$$

leads to the determination of the parameter α, and then gives the allowed wave number q. This algorithm is similar to the case for ferromagnetic thin films [14–16].

The SSW is obtained by superposition of two waves propagating into the opposite directions,

$$\chi(\bar{z},\tau) = \frac{\nu_q(\bar{z}_{L/2+z}) + \nu_q(\bar{z}_{L/2-z})}{\nu_q(\bar{z}_L) + \nu_q(\bar{z}_0)}\chi(\bar{z}_{L/2},\tau). \tag{21}$$

We obtain a similar expression for $\psi(\bar{z},\tau)$. Here, the boundary functions are taken from the numerical data. In Fig. 6, we show a comparison between numerical and analytical results for the spatial profiles of (a) φ and (b) θ associated with the first-order standing waves over the CSL structure under a finite dc magnetic field ($\beta_0 = 0.002$). It is seen that the analytical results are consistent with the numerical ones.

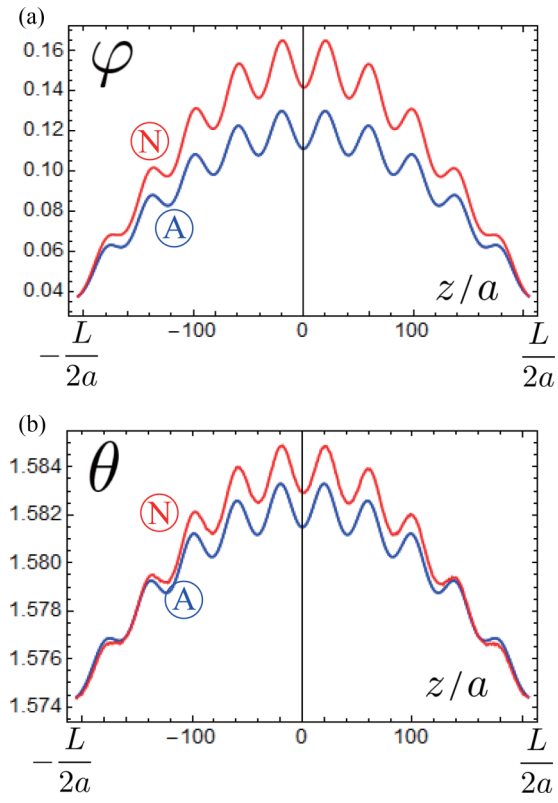

FIG. 6. Comparison between numerical (red line) and analytical (blue line) results for the spatial profiles of (a) φ and (b) θ associated with the first-order standing waves over the CSL structure under a finite dc magnetic field ($\beta_0 = 0.002$). The parameters are taken as $\beta_{\rm s} = 0.02$ and $\beta_{x0} = 0.0001$. An analytical result is obtained from Eq. (21) at $\tau = 5600$.

Analytical results enable us to understand the origin of the ripples. For this purpose, we decompose Eq. (18) into a "Bloch wave" ($e^{-i\bar{q}\bar{z}}$) and a "Lamé ripple" $[\theta_4(\frac{\pi}{2K}[\bar{z} - i\alpha - K])/\theta_4(\frac{\pi\bar{z}}{2K})]$. We separately show the spatial profiles of these waves in Fig. 7. It is seen that the Bloch part behaves like a smooth background, while the Lamé part exhibits the short-wavelength modulation (ripple), which directly reflects the spatial period of the CSL, $L_{\rm CSL}$.

Figure 8 shows the spectrum of the SSW of the first, second, and third orders, where both numerical and analytical results are shown for comparison. It is evident that the theoretical and numerical results are in good agreement.

2. *SSW over the simple helix*

In this subsection we discuss separately the case of a zero magnetic dc field ($\beta_0 = 0$). In this case, the ground state

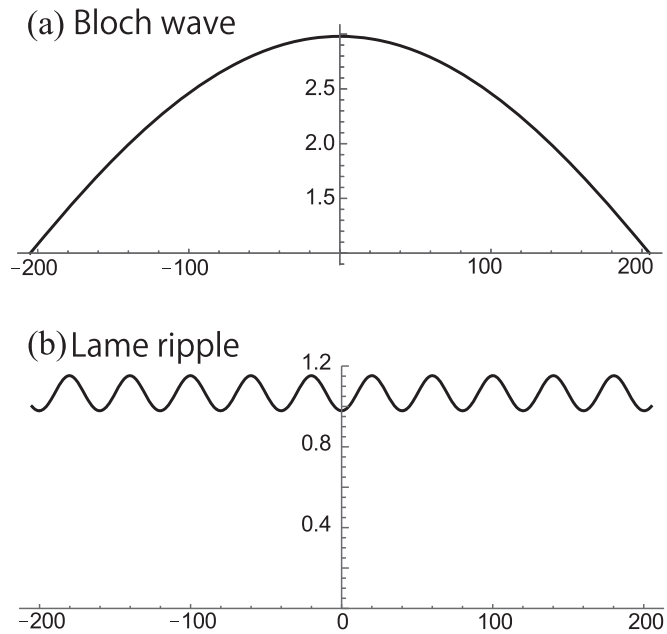

FIG. 7. Schematic demonstration of how the SSW wave function over the CSL, Eq. (18), is decomposed into (a) a Bloch wave ($e^{-i\bar{q}\bar{z}}$) and (b) Lamé ripple $[\theta_4(\frac{\pi}{2K}[\bar{z} - i\alpha - K])/\theta_4(\frac{\pi\bar{z}}{2K})]$. The parameter setting is the same as in the case of Fig. 6.

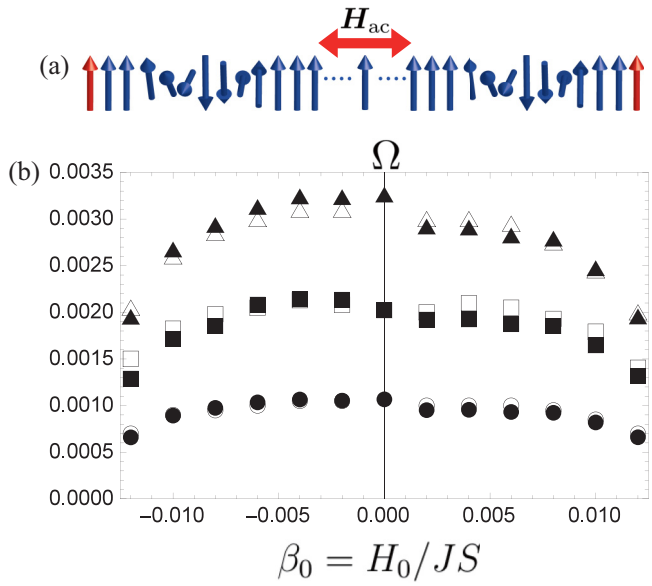

FIG. 8. (a) Schematic view of the case I configuration. (b) Resonance frequency Ω_0 for standing waves of the first order (◯, numerical data; ●, theory), the second order (□, numerical data; ■, theory), and the third order (△, numerical data; ▲, theory) depending on the transverse dc field β_0.

is a simple helix with a uniform modulation and the above analysis can be repeated in a much simpler manner [11].

The helical structure of the interior spins is described by $\theta_0 = \pi/2$ and $\varphi_0 = q_s(z - z_0)$. The helical pitch is determined through an equation (see Appendix B for derivation)

$$0 = \sin q_s - (D/J)\cos q_s \mp \beta_s \sin\varphi(\mp L/2). \tag{22}$$

The presence of the pinning field complicates the condition for q_s.

The equations of motion (7) and (8) may be recast in the form

$$\partial_\tau \psi = -\partial_z^2 \chi, \tag{23}$$

$$\partial_\tau \chi = \left[\partial_z^2 - 2(D/J)q_s + q_s^2\right]\psi - \beta_z(\tau). \tag{24}$$

We look for solutions in the form of the standing wave, $\cos(kz)$, with the wave vector k. The resonance frequency for the interior spins is then given by

$$\Omega^2_{\text{interior}} = k^2\left[k^2 - q_s^2 + 2q_s(D/J)\right]. \tag{25}$$

On the other hand, the resonance frequency for the surface end spins is obtained as

$$\begin{aligned}\Omega^2_{\text{surface}} = {} & [k\tan(kL/2)\{1 + (D/J)q_s\} \\ & - k^2/2 - \beta_s\cos\varphi_0(L/2)] \\ & \times \{k\tan(kL/2) - k^2/2 + q_s^2/2 \\ & - (D/J)q_s - \beta_s\cos\varphi_0(L/2)\}.\end{aligned} \tag{26}$$

Then, the Davis-Puszkarski equation leads to the determination of allowed values of k.

By performing numerical estimations for $D/J = 0.16$, $\beta_s = 0.02$, and $\varphi_0(\mp L/2) = \pm 31.6369$, where $L/2 = 205$, we obtain $k^{(1)} = 0.006\,671$, $\Omega_0^{(1)} = 0.001\,067$ and $k^{(3)} = 0.020\,279$, $\Omega_0^{(3)} = 0.003\,268$ for the standing waves of the first and third orders, respectively [38]. This result is included in Fig. 8.

B. Case II: The ac magnetic field is perpendicular to the chiral axis

1. SSW over the CSL

Now we examine the most complicated case, where the SSW is excited over the CSL by the ac field applied perpendicular to the chiral axis. To the best of our knowledge, such a study had not yet been conducted. An essential feature of this case lies in the fact that the interior spins experience space-time-dependent Zeeman interaction with an effective field $\beta_{\text{eff}}(z,\tau) = \sin\varphi_0(z)\beta_x(\tau)$ in Eq. (7). This term prevents us from applying a separation of variables. To attack the problem, the method of transformations leading to homogeneous boundary conditions may be used [40]. For the purpose, we solve initially the EOM for the interior spins by assuming that dynamics of the end spins is known. The results obtained in this fashion are then used to address the problem to describe the dynamics of the end surface spins in a self-consistent manner.

To realize the scheme, the spin fluctuations may be expanded as

$$\chi(\bar{z},\tau) = \frac{\nu_q(\bar{z})}{\nu_q(\bar{z}_{L/2})}\chi(\bar{z}_{L/2},\tau) + \epsilon\tilde{\chi}(\bar{z},\tau), \tag{27}$$

$$\psi(\bar{z},\tau) = \frac{\nu_q(\bar{z})}{\nu_q(\bar{z}_{L/2})}\psi(\bar{z}_{L/2},\tau) + \epsilon\tilde{\psi}(\bar{z},\tau), \tag{28}$$

where the first terms correspond to the standing-wave antisymmetric with respect to reflection across the center,

$$\nu_q(\bar{z}) \propto \text{Im}\left[\frac{\theta_4\left(\frac{\pi}{2K}[\bar{z} - i\alpha - K]\right)}{\theta_4\left(\frac{\pi\bar{z}}{2K}\right)}e^{-i\bar{q}\bar{z}}\right]. \tag{29}$$

The second terms on the right-hand side of Eqs. (27) and (28) give rise to the additional short-wavelength ripples with both ends being completely pinned, i.e., $\tilde{\chi}(\bar{z}_{\pm L/2},\tau) = 0$ and $\tilde{\psi}(\bar{z}_{\pm L/2},\tau) = 0$. In view of the complete pinning, we call this additional ripple the "Kittel ripple."

The amplitude of the Kittel ripple is proportional to the small parameter ϵ. From the beginning, the dynamics of the end spins, i.e., $\chi(\bar{z}_{L/2},\tau)$ and $\psi(\bar{z}_{L/2},\tau)$, is considered as being known. Due to the odd parity of the function $\nu_q(\bar{z})$, the oscillations of the boundary spins are antisynchronized, i.e., $\chi(\bar{z}_{-L/2},\tau) = -\chi(\bar{z}_{L/2},\tau)$ and $\psi(\bar{z}_{-L/2},\tau) = -\psi(\bar{z}_{L/2},\tau)$.

Substituting Eqs. (27) and (28) into Eqs. (7) and (8), we obtain the coupled equations of zeroth-order in ϵ,

$$\dot{\psi}(\bar{z}_{L/2},\tau) = (\beta_0/\kappa^2)\lambda^{(\varphi)}\chi(\bar{z}_{L/2},\tau), \tag{30}$$

$$\dot{\chi}(\bar{z}_{L/2},\tau) = -(\beta_0/\kappa^2)\lambda^{(\theta)}\psi(\bar{z}_{L/2},\tau), \tag{31}$$

which gives the resonance frequency for the Pincus mode of the interior spins,

$$\begin{aligned}\Omega^2_{\text{interior-Pincus}} = \frac{\beta_0^2}{\kappa^4}\lambda^{(\varphi)}\lambda^{(\theta)} = {} & \frac{\beta_0^2}{\kappa^4}\kappa'^2\text{sn}^2(\alpha,\kappa') \\ & \times [\kappa'^2\text{sn}^2(\alpha,\kappa') + 2 + 2\kappa'^2],\end{aligned} \tag{32}$$

with no restriction on α. We call this the "interior Pincus" mode.

The coupled equations of the first-order in ϵ are found to be

$$\dot{\tilde{\psi}}(\bar{z},t) = \frac{\beta_0}{\kappa^2}\hat{\mathcal{L}}_\varphi \tilde{\chi}(\bar{z},t) + \frac{\beta_x(\tau)}{\epsilon}\sin\varphi_0(\bar{z}), \tag{33}$$

$$\dot{\tilde{\chi}}(\bar{z},t) = -\frac{\beta_0}{\kappa^2}\hat{\mathcal{L}}_\theta \tilde{\psi}(\bar{z},t). \tag{34}$$

The resonance frequency for the Kittel ripples of the interior spins is now

$$\Omega^2_{\text{interior-Kittel}}(q) = \frac{\beta_0^2}{\kappa^4}\kappa'^2 \mathrm{sn}^2(\alpha,\kappa') \times [\kappa'^2 \mathrm{sn}^2(\alpha,\kappa') + 2 + 2\kappa'^2], \tag{35}$$

under the restriction on α due to the boundary condition, $\nu_q(\bar{z}_{\pm L/2}) = 0$. We look for solutions of Eqs. (33) and (34) in the form

$$\tilde{\psi}(\bar{z},\tau) = \sum_n \tilde{\psi}_n(\tau)\nu_{q_n}(\bar{z}), \tag{36}$$

$$\tilde{\chi}(\bar{z},\tau) = \sum_n \tilde{\chi}_n(\tau)\nu_{q_n}(\bar{z}), \tag{37}$$

where the wave vectors q_n are determined by $\nu_{q_n}(\bar{z}_{\pm L/2}) = 0$.

Inserting Eqs. (36) and (37) into Eqs. (33) and (34) yields

$$\tilde{\chi}_n(\tau) = f_n \frac{\beta_{x0}}{\epsilon}\frac{\kappa^2}{\beta_0}\frac{\Omega_n}{\lambda_n^{(\varphi)}}\frac{[\Omega_n \sin(\Omega\tau) - \Omega\sin(\Omega_n\tau)]}{\Omega^2 - \Omega_n^2}, \tag{38}$$

$$\tilde{\psi}_n(\tau) = f_n \frac{\beta_{x0}}{\epsilon}\Omega\frac{[\cos(\Omega_n\tau) - \cos(\Omega\tau)]}{\Omega^2 - \Omega_n^2}, \tag{39}$$

where Ω_n is given by (35) being estimated for q_n, and

$$f_n = \frac{\int_{-\bar{z}_{L/2}}^{\bar{z}_{L/2}} \sin\varphi_0(\bar{z})\nu_{q_n}(\bar{z})d\bar{z}}{\int_{-\bar{z}_{L/2}}^{\bar{z}_{L/2}} \nu_{q_n}^2(\bar{z})d\bar{z}}. \tag{40}$$

The function $\sin\varphi_0$ is antisymmetric with respect to reflection across the center of the system, and therefore the summation in (36) and (37) should include the odd functions $\nu_{q_n}(\bar{z})$ only.

In Fig. 9, we show a comparison between numerical and analytical results for the spatial profiles of φ and θ associated with the second-order standing waves over the CSL structure under a finite dc magnetic field.

We now consider the boundary values $\chi(\bar{z}_{L/2},\tau)$ and $\psi(\bar{z}_{L/2},\tau)$. To do this in a self-consistent manner, we neglect the additional Kittel ripple terms in Eqs. (27) and (28), which become vanishingly small in the vicinity of the boundaries,

$$\chi(\bar{z},\tau) \sim c_\chi \frac{\nu_q(\bar{z})}{\nu_q(\bar{z}_{L/2})}\chi(\bar{z}_{L/2},\tau), \tag{41}$$

$$\psi(\bar{z},\tau) \sim c_\psi \frac{\nu_q(\bar{z})}{\nu_q(\bar{z}_{L/2})}\psi(\bar{z}_{L/2},\tau), \tag{42}$$

where c_χ and c_ψ are some constants.

Substitution of (41) and (42) into Eqs. (9) and (10) leads to the differential equations for the two unknowns $\psi(z_{L/2},\tau)$ and $\chi(z_{L/2},\tau)$,

$$\dot{\psi}(z_{L/2},\tau) = -\frac{c_\chi}{c_\psi}A_q\chi(z_{L/2},\tau) + \frac{\beta_x(\tau)}{c_\psi}\sin\varphi_0(z_{L/2}), \tag{43}$$

$$\dot{\chi}(z_{L/2},\tau) = \frac{c_\psi}{c_\chi}B_q\psi(z_{L/2},\tau), \tag{44}$$

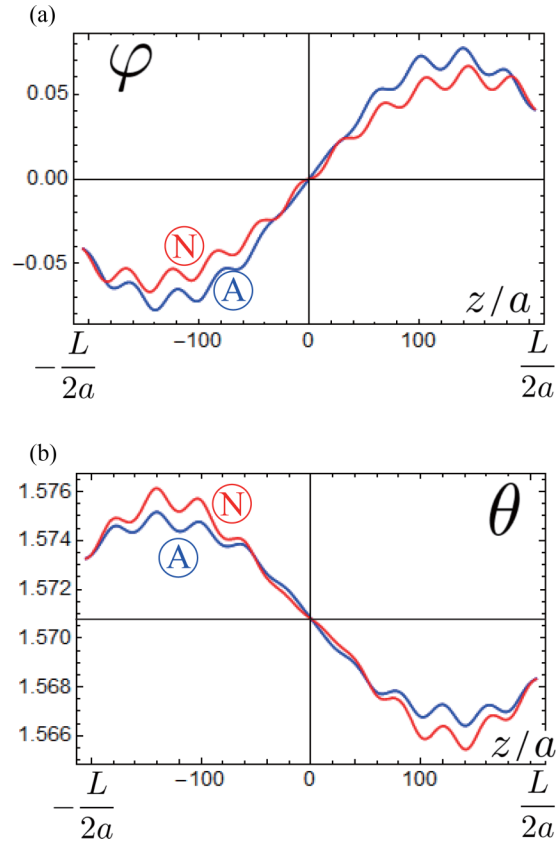

FIG. 9. Comparison between numerical (red line) and analytical (blue line) results for the spatial profiles of (a) φ and (b) θ associated with the second-order standing waves over the CSL structure under a finite dc magnetic field ($\beta_0 = 0.002$). The parameters are taken as $\beta_s = 0.02$ and $\beta_{x0} = 0.0001$. An analytical result is obtained by Eqs. (27) and (28) with $\epsilon = 2/3$ at $\tau = 6000$.

where

$$A_q = -\frac{\nu_q'(z_{L/2})}{\nu_q(z_{L/2})} + \frac{1}{2}\frac{\nu_q''(z_{L/2})}{\nu_q(z_{L/2})} + \frac{D}{J}\frac{\nu_q'(z_{L/2})}{\nu_q(z_{L/2})}\varphi_0'(z_{L/2}) - (\beta_s + \beta_0)\cos\varphi_0(z_{L/2}), \tag{45}$$

$$B_q = -\frac{\nu_q'(z_{L/2})}{\nu_q(z_{L/2})} + \frac{1}{2}\frac{\nu_q''(z_{L/2})}{\nu_q(z_{L/2})} + \frac{1}{2}\varphi_0'^2(z_{L/2}) + \frac{D}{J}\varphi_0'(z_{L/2}) - \frac{D}{2J}\varphi_0''(z_{L/2}) - (\beta_s + \beta_0)\cos\varphi_0(z_{L/2}). \tag{46}$$

Then, the resonance frequency for the end surface spins is

$$\Omega_{\text{surface-Pincus}} = \sqrt{A_q B_q}, \tag{47}$$

which is identified as the "surface Pincus" mode. Choosing the initial values $\psi(z_{L/2},0) = 0$ and $\chi(z_{L/2},0) = 0$

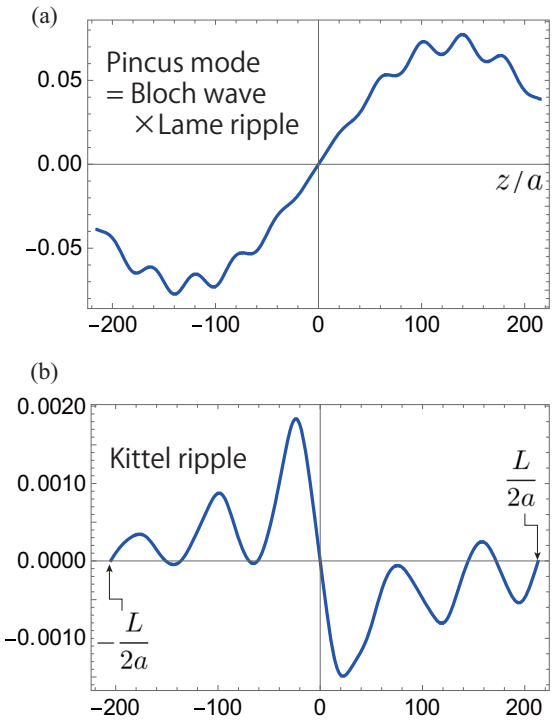

FIG. 10. Decomposition of Eq. (27) into the (a) Pincus mode (which is further decomposed into the Bloch wave and Lamé ripple, as shown in Fig. 7) and (b) Kittel ripples.

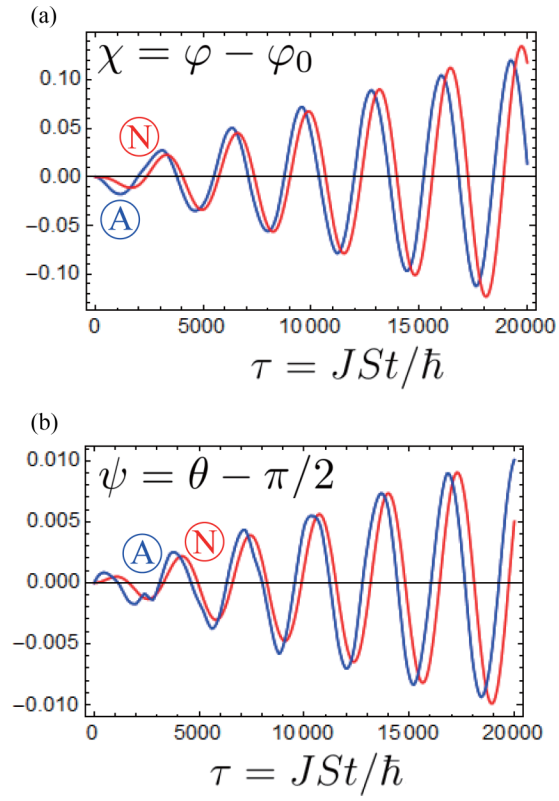

FIG. 11. Time evolution of $\chi(L/2,\tau)$ and $\psi(L/2,\tau)$: numerical data (blue) and the analytical relation (49) and (48), respectively, (red) with $c_\chi = 60$ and $c_\psi = -32$.

that are consistent with the field $\beta_x(\tau) = \beta_{x0}\sin(\Omega\tau)$, we find

$$\chi(z_{L/2},\tau) = \frac{\beta_{x0}B_q}{c_\chi}\frac{\sin\varphi_0(z_{L/2})}{\Omega_0\left(\Omega_0^2-\Omega^2\right)}[\Omega_0\sin(\Omega\tau)-\Omega\sin(\Omega_0\tau)], \tag{48}$$

$$\psi(z_{L/2},\tau) = \frac{\beta_{x0}}{c_\psi}\frac{\Omega\sin\varphi_0(z_{L/2})}{\Omega^2-\Omega_0^2}[\cos(\Omega_0\tau)-\cos(\Omega\tau)], \tag{49}$$

where $\Omega_0 = \Omega_{\text{surface-Pincus}} = \Omega_{\text{interior-Pincus}}$. This matching condition leads to the determination of the wave number q.

Analytical results obtained here enable us to understand how the SSWs are constructed from the Bloch waves, Lamé ripples, and Kittel ripples. In Fig. 10, we separately show the spatial profile of $\chi(\bar{z}_{L/2},\tau)$ and $\epsilon\tilde{\chi}(\bar{z},\tau)$ in Eq. (27). The Pincus modes consist of the slowly varying Bloch wave and short-wavelength Lamé ripple. On the other hand, the Kittel ripple is completely pinned down at both ends and has a tiny amplitude.

To make a supplementary comparison between numerical and analytical results, in Fig. 11 we show the time evolution of $\chi(L/2,\tau)$ and $\psi(L/2,\tau)$. The analytical results are given by Eqs. (49) and (48).

Finally, computation of $\tilde{\chi}$ and $\tilde{\psi}$ with the aid of the found solutions gives resonances of the Kittel ripples at Ω_n. In Fig. 12, we summarize the results that are the most essential results in this paper to make a comparison between theoretical and experimental findings on the magnetic resonance in case II.

In Fig. 12(c), it is seen that there appear double resonances. The lower branch originates from the lowest antisymmetric Pincus mode of the second order ($M = 2$) and the upper branch originates from the lowest Kittel ripple with $n = 1$. Actually, the first and second resonance frequencies are reported as $\Omega_1 \sim 17$ GHz and $\Omega_2 \sim 20$ GHz with the bell-shaped field dependence, i.e., $(\Omega_2 - \Omega_1)/\Omega_1$ is the order of 0.1. Based on this fact, we may conclude that the experimentally observed double resonances consistently correspond to the second Pincus mode and the first Kittel ripple mode, respectively. The difference in the resonance frequencies between the first and second Pincus modes [shown in Fig. 12(b)] is too large as compared with the experimental finding. As for direct quantitative comparison between the theory and the reported experimental results, we mark that $\Omega \sim 0.002$ for the lowest antisymmetric mode corresponds to $(JS/\hbar)\Omega \sim 7$ GHz in physical units, i.e., approximately half as much as detected in experiments. To justify the discrepancy, we mention that the resonant frequency is inversely proportional to the square root of the system size, $\Omega \sim L^{-1/2}$, as proved early in Ref. [7]. That means that the length of the system should be reduced to $L \sim 100$ in order to achieve an agreement with the experimental values. However, it must be remembered that an accurate estimate of the pinning field is required for such a direct comparison. Another important factor totally neglected in our analysis is an easy-plane anisotropy, which is present in $CrNb_3S_6$ [39], which can increase the resonant frequency also [8].

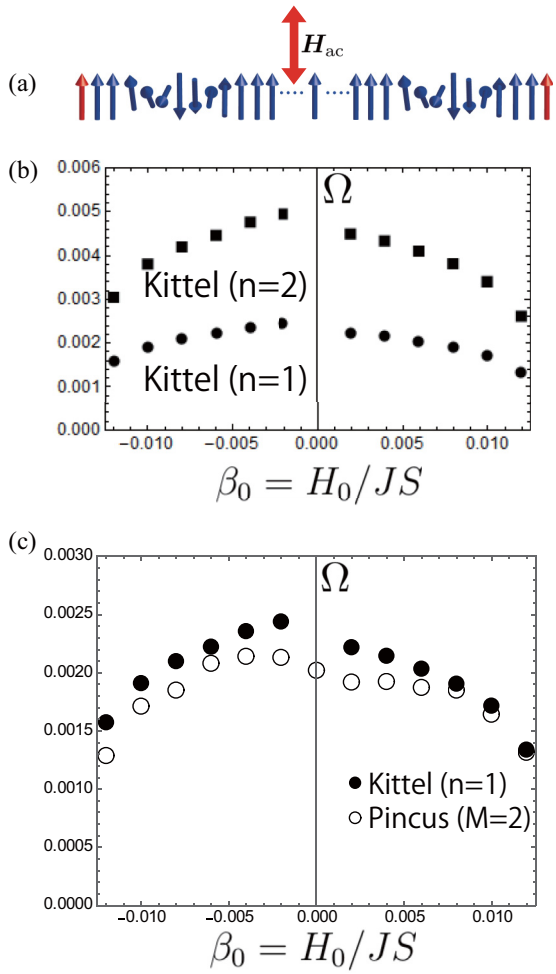

FIG. 12. (a) Schematic view of the case II configuration. (b) Resonance frequencies for the Kittel ripples of the lowest orders $n = 1$ and 2 shown by ● and ■, respectively. (c) H_0 dependences of the lowest antisymmetric $M = 2$ Pincus mode (○) and the $n = 1$ ripple Kittel mode (●).

We also note that the intensities of the Pincus mode and Kittel ripples are almost similar, because they are both the fundamental modes. Based on these considerations, we may conclude that the resonance profile in case II is attributed to the coexistence of the Pincus and Kittel excitations. In the final part of Appendix C, we explained the reason why the resonance frequency for the Pincus mode is smaller than that of the Kittel ripple.

The asymmetric profile of the distribution of the resonance frequencies with respect to the direction of the dc field ($\beta_0 > 0$ or $\beta_0 < 0$) should be discussed in more detail. This asymmetry is actually observed experimentally [10]. At first glance, the origin of this characteristic could easily be attributed to the pinning field at both ends. Because the pinning fields $\boldsymbol{H}_s$ are uniform, the total field, $\boldsymbol{H}_0 + \boldsymbol{H}_s$, exhibits an asymmetric profile depending on the orientation of $\boldsymbol{H}_0$, i.e., the $\boldsymbol{H}_0$ is either parallel or antiparallel to the $\boldsymbol{H}_s$. It should, however, be recognized that this explanation is not fully satisfactory, being a consequence of the time-reversal symmetry breaking arising when replacing magnetic anisotropy with a fictitious "surface" field. Apparently, this problem demands clarification, therefore we mention the experimental fact that may serve as a key to addressing the challenge. Namely, investigations of magnetic structure near grain boundaries of $CrNb_3S_6$ thin films reveal two $\pi/2$ twists that connect in-plane spins on either side of the boundary. The $\pi/2$ twist spin configuration looks like that found in MnSi thin films [27,41] and is related to the continuity of a normal component of the Poynting vector at the boundary surface [42].

2. *SSW over the simple helix*

Similar to case I, the case of a simple helix can be more easily analyzed than the case of the CSL. In case II, the SSW is antisymmetric with respect to reflection across the center. This situation reminds us of the standing waves in thin ferromagnetic films with the asymmetric surface pinning [15]. We accordingly modify the scheme given by Eqs. (27) and (28) in the form

$$\chi(z,\tau) = \frac{\sin(kz)}{\sin(kL/2)}\chi(L/2,\tau) + \varepsilon\tilde{\chi}(z,\tau), \tag{50}$$

$$\psi(z,\tau) = \frac{\sin(kz)}{\sin(kL/2)}\psi(L/2,\tau) + \varepsilon\tilde{\psi}(z,\tau). \tag{51}$$

Apparently, the boundary values become antisymmetric, $\chi(-L/2,\tau) = -\chi(L/2,\tau)$ and $\psi(-L/2,\tau) = -\psi(L/2,\tau)$, provided the short-range parts vanish at the end.

We make use of (50) and (51) for the system

$$\partial_\tau\psi = -\partial_z^2\chi + \beta_x(\tau)\sin(q_s z), \tag{52}$$

$$\partial_\tau\chi = \left[\partial_z^2 - 2(D/J)q_s + q_s^2\right]\psi, \tag{53}$$

and we seek the solution in the form of the Fourier series

$$\tilde{\psi}(z,\tau) = \sum_{n=1}^{\infty}\tilde{\psi}_n(\tau)\sin(2\pi nz/L), \tag{54}$$

$$\tilde{\chi}(z,\tau) = \sum_{n=1}^{\infty}\tilde{\chi}_n(\tau)\sin(2\pi nz/L). \tag{55}$$

Here,

$$\tilde{\chi}_n(\tau) = f_n\frac{\beta_{x0}}{\epsilon}\sqrt{\frac{q_n^2 - q_s^2 + 2q_s(D/J)}{q_n^2}} \times \frac{[\Omega_n\sin(\Omega\tau) - \Omega\sin(\Omega_n\tau)]}{\Omega^2 - \Omega_n^2}, \tag{56}$$

$$\tilde{\psi}_n(\tau) = f_n\frac{\beta_{x0}}{\epsilon}\Omega\frac{[\cos(\Omega_n\tau) - \cos(\Omega\tau)]}{\Omega^2 - \Omega_n^2} \tag{57}$$

with the coefficients being given by

$$f_n = \frac{2}{L}\int_{-L/2}^{L/2}\sin(q_s z)\sin(2\pi nz/L)dz. \tag{58}$$

The wave vectors are given by $q_n = 2\pi n/L$ such that $\sin(q_n L/2) = 0$. The resonance frequency for the Kittel ripple is then given by

$$\Omega_n^2 = q_n^2\left[q_n^2 - q_s^2 + 2q_s(D/J)\right]. \tag{59}$$

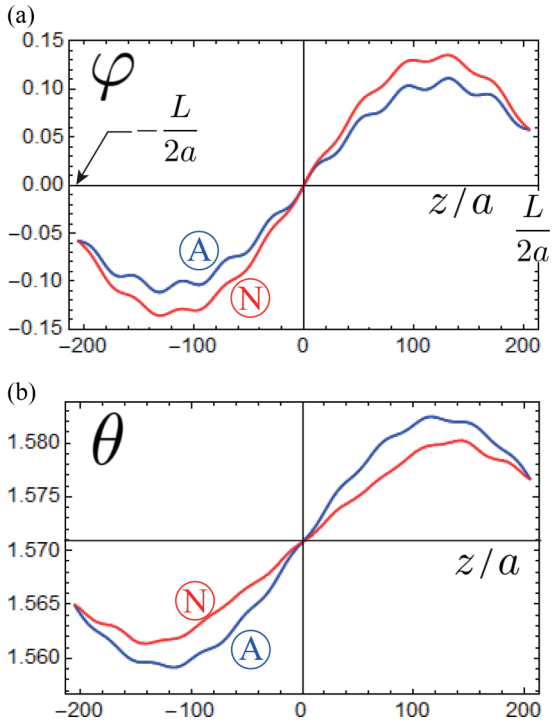

FIG. 13. Comparison between numerical (red line) and analytical (blue line) results for the spatial profiles of (a) φ and (b) θ associated with the second-order standing waves over the helical structure under zero dc magnetic field ($\beta_0 = 0$). The parameters are taken as $\beta_s = 0.02$ and $\beta_{x0} = 0.0001$. An analytical result is obtained from Eqs. (50) and (51) with $\epsilon = -2/3$ at $\tau = 9500$.

On the other hand, the resonance frequency for the Pincus mode is obtained through

$$\begin{aligned}&[k\cot(kL/2)(1-q_sD/J)+k^2/2+\beta_s\cos(kL/2)]\\&\quad\times\left[k\cot(kL/2)+k^2/2-q_s^2/2\right.\\&\quad\left.-(D/J)q_s+\beta_s\cos(kL/2)\right]\\&=k^2\left[k^2-q_s^2+2q_s(D/J)\right].\end{aligned}\tag{60}$$

Numerical estimates with the same parameters as in the previous subsection give the value $k^{(2)} = 0.012\,603\,8$. In Fig. 13, we show a comparison between the numerical and analytical results.

To specify boundary dynamics, we substitute

$$\chi(\bar{z},\tau)\sim c_\chi\frac{\sin(kz)}{\sin(kL/2)}\chi(L/2,\tau),\tag{61}$$

$$\psi(z,\tau)\sim c_\psi\frac{\sin(kz)}{\sin(kL/2)}\psi(L/2,\tau)\tag{62}$$

into Eqs. (9) and (10), which yields

$$\chi(z_{L/2},\tau)=\frac{\beta_{x0}}{c_\chi}\frac{B_k\sin\varphi_0(z_{L/2})}{\Omega_0\left(\Omega_0^2-\Omega^2\right)}[\Omega_0\sin\Omega\tau-\Omega\sin\Omega_0\tau],\tag{63}$$

$$\psi(z_{L/2},\tau)=\frac{\beta_{x0}}{c_\psi}\frac{\Omega\sin\varphi_0(z_{L/2})}{\left(\Omega^2-\Omega_0^2\right)}[\cos\Omega_0\tau-\cos\Omega\tau],\tag{64}$$

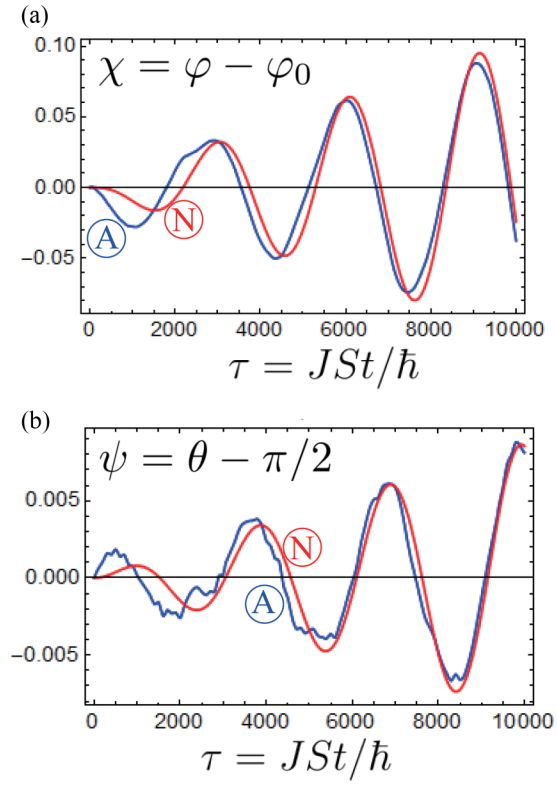

FIG. 14. Time evolution of $\chi(L/2,\tau)$ and $\psi(L/2,\tau)$: numerical data (blue) compared to the analytical relations (49) and (48), respectively, (red) with $c_\chi = -12.5$ and $c_\psi = -19.0$.

where

$$B_k=-k\cot(kL/2)-k^2/2+q_s^2/2+(D/J)q_s-\beta_s\cos(kL/2).\tag{65}$$

These results show that the end spins oscillate with the frequency of an unperturbed standing wave,

$$\Omega_0^2=k^2\left[k^2-q_s^2+2q_s(D/J)\right],\tag{66}$$

where the numerical estimation gives $\Omega_0 \approx 0.002\,018\,5$. For comparison, the lowest short-range ripple frequency is $\Omega_1 = 0.002\,461\,7$. Figures 14(a) and 14(b) illustrate comparison of (63) and (64) with numerical data.

V. DISCUSSIONS AND CONCLUSIONS

In this paper, motivated by experimental findings on the magnetic-field dependence of the resonance profile in $CrNb_3S_6$ [10], we developed a theory of the SSW in a monoaxial chiral helimagnet. We assumed that microsized samples used in Ref. [10] are described as thin films with both the surface end spins being softly pinned, and we constructed a theory along with the line of Kittel-Pincus theories of ferromagnetic resonance. From technical viewpoints, we presented a scheme of the Davis-Puszkarski equation generalized to the case of chiral helimagnetic structure under the static magnetic field applied perpendicular to the chiral axis.

Consequently, we found there are two classes of the SSW over the spatially modulated chiral spin soliton lattice state. One is the soft Pincus mode, while another is the hard Kittel ripple. The former is analogous to the SSW in a ferromagnetic

thin film discussed by Pincus [13]. The latter appears only in the case of a spatially modulated spin structure, because the spatially oscillating field acts on the interior spins and causes forced oscillation in the space-domain. The Kittel ripples are excited only when the ac magnetic field is applied perpendicular to the chiral axis, because the perpendicular field couples with the spatially modulated component of the spins through the term $\beta_x(t)\cos\varphi_0(z)$. The existence of two modes, the Pincus modes and Kittel ripples, is consistent with the experimentally observed double-resonance profile.

Standing spin waves in thin ferromagnetic films have been studied intensively from both theoretical and experimental standpoints. These excitations have already found a broad application in problems of spintronics. However, to the best of our knowledge, the problem of the SSW for a noncollinear magnetic structure has not been addressed so far. The present paper may open a new direction in the field.

Finally, we make some general comments on the issues that have not been addressed in this paper. Generally speaking, consideration of the chiral helimagnets requires careful treatment of dipole-exchange and magnetostatic modes, which play an essential role in films of thickness typically in the range of micrometers [43–45]. Measurements in $CrNb_3S_6$ samples of finite geometries show that the overall resonance response depends on nonuniform magnetization fields [11]. Their account has been done only for the phase of forced ferromagnetism, but there remains a need for similar study in the CSL phase.

Another important aspect involved in practical application of the standing spin waves pertains to accounting for damping effects not dealt with in this work. The theoretical studies for thin films of an itinerant ferromagnet have shown that the Landau damping mechanism of the standing-wave modes is sufficiently severe, since they have a finite and rather large vector normal to the film surfaces [46]. An analysis of the perpendicular standing waves in sputtered permalloy films by means of waveguide-based FMR measurements identifies three contributions to their damping: the intrinsic damping, the eddy-current damping [47], and the radiative damping that stem from the inductive coupling between the sample and the waveguide [48]. The radiative damping is present in all ferromagnets including insulators.

The eddy-current damping may materialize for standing waves in $CrNb_3S_6$ films, since there are itinerant carriers from conducting NbS_2 layers. However, even studies in itinerant ferromagnets, quite thick permalloy films, demonstrate that the eddy-current damping may be neglected in higher-order standing waves. In addition, in thin ferromagnetic films the eddy-current damping was found to be negligible in comparison with the wave-number-dependent damping mechanism due to intralayer spin-current transport [49]. Further theoretical and experimental exploration toward this direction is of interest for future investigations.

ACKNOWLEDGMENTS

The authors thank E.A. Elfimova, Y. Kato, and J. Ohe for fruitful discussions. This work was supported by a Grant-in-Aid for Scientific Research (B) (No. 17H02923) from the MEXT of the Japanese Government, JSPS Bilateral Joint Research Projects (JSPS-FBR), and the JSPS Core-to-Core Program, A. Advanced Research Networks. Vl.E.S. and I.P. acknowledge financial support by the Ministry of Education and Science of the Russian Federation, Grant No. MK-1731.2018.2 and by the Russian Foundation for Basic Research (RFBR), Grant No. 18-32-00769 (mol_a). A.S.O. and I.G.B. acknowledge funding by the RFBR, Grant No. 17-52-50013, by the Foundation for the Advancement of Theoretical Physics and Mathematics BASIS Grant No. 17-11-107, and by Act 211 Government of the Russian Federation, Contract No. 02.A03.21.0006. A.S.O. thanks the Ministry of Education and Science of the Russian Federation, Project No. 3.2916.2017/4.6.

APPENDIX A: LAMÉ FORM OF EQUATIONS OF MOTION

We derive here Eqs. (7) and (8). First, in Eqs. (3) and (4), we make a linear expansion with respect to ψ and χ to obtain

$$\begin{aligned}
\sin\theta\partial_z^2\varphi &\to \partial_z^2\varphi_0 + \partial_z^2\chi,\\
\beta_0\sin\varphi &\to \beta_0\sin\varphi_0 + (\beta_0\cos\varphi_0)\chi,\\
\beta_x\sin\varphi &\to \beta_x\sin\varphi_0,\\
\sin\theta\cos\theta(\partial_z\varphi)^2 &\to -\psi(\partial_z\varphi_0)^2,\\
\sin\theta\cos\theta\partial_z\varphi &\to -\psi\partial_z\varphi_0,
\end{aligned}$$

where we note that φ_0 satisfies the sine-Gordon equation, $\partial_z^2\varphi_0 = \beta_0\sin\varphi_0$. The higher-order terms such as $\psi\partial_z\psi$, $\beta_x\chi$, and $\beta_x\psi$ are discarded (β_x is treated as a small perturbation). Plugging them into Eqs. (3) and (4) and introducing dimensionless space and time variables, $\bar{z} = z\sqrt{\beta_0}/\kappa$ and $\tau = JSt/\hbar$, we have

$$\frac{\kappa^2}{\beta_0}\partial_\tau\psi = \left(-\frac{\partial^2}{\partial\bar{z}^2} + \kappa^2\cos\varphi_0\right)\chi + \frac{\kappa^2}{\beta_0}\beta_x(\tau)\sin\varphi_0, \tag{A1}$$

$$\begin{aligned}
\frac{\kappa^2}{\beta_0}\partial_\tau\chi = -\Bigg[&-\frac{\partial^2}{\partial\bar{z}^2} + \kappa^2\cos\varphi_0 - (\partial_{\bar{z}}\varphi_0)^2\\
&+2\frac{D}{J}\frac{\kappa}{\sqrt{\beta_0}}(\partial_{\bar{z}}\varphi_0)\Bigg]\psi - \frac{\kappa^2}{\beta_0}\beta_z(\tau).
\end{aligned} \tag{A2}$$

Using Eq. (5), it may be shown that

$$\cos\varphi_0 = -1 + 2\,\mathrm{sn}^2\bar{z}, \tag{A3}$$

$$\partial_{\bar{z}}\varphi_0 = 2\,\mathrm{dn}\bar{z}. \tag{A4}$$

and Eq. (A1) is reduced to Eq. (7). For small κ, we can approximate

$$\frac{\kappa}{\sqrt{\beta_0}} = \frac{4JE(\kappa)}{\pi D} \sim \frac{2J}{D}\left(1 - \frac{\kappa^2}{4}\right), \tag{A5}$$

$$\mathrm{dn}\bar{z} = \sqrt{1-\kappa^2\mathrm{sn}^2\bar{z}} \sim 1 - \frac{\kappa^2}{2}\mathrm{sn}^2\bar{z}. \tag{A6}$$

Then, Eq. (A2) is reduced to

$$\begin{aligned}
\frac{\kappa^2}{\beta_0}\partial_\tau\chi = -&\left(-\frac{\partial^2}{\partial\bar{z}^2} + 2\kappa^2\mathrm{sn}^2\bar{z} - 3\kappa^2 + 4\right)\psi\\
&- \frac{\kappa^2}{\beta_0}\beta_z(\tau),
\end{aligned} \tag{A7}$$

which gives Eq. (8).

APPENDIX B: DYNAMICS OF THE SURFACE END SPINS

We examine in detail the motion of the end spins with the coordinates $\pm L/2$ in a line of N spins along the z axis. It is assumed that the end spins experience an effective "surface" anisotropy field H_s, the same on both ends, which is perpendicular to the line and to the static magnetic field H_0.

The boundary spins differ from interior ones in that they have only one nearest neighbor instead of the usual two, thereby giving the Hamiltonian for the right end spin

$$\mathcal{H}_R = -J\boldsymbol{S}_{L/2-1}\cdot\boldsymbol{S}_{L/2} - D[\boldsymbol{S}_{L/2-1}\times\boldsymbol{S}_{L/2}]_z - (H_0+H_s)S^x_{L/2}. \tag{B1}$$

The equations of motion are then shaped into

$$\begin{aligned}\partial_\tau\theta_{L/2} &= \sin\theta_{L/2-1}\sin(\varphi_{L/2}-\varphi_{L/2-1}) \\ &\quad -(D/J)\sin\theta_{L/2-1}\cos(\varphi_{L/2}-\varphi_{L/2-1}) \\ &\quad +(\beta_0+\beta_s)\sin\varphi_{L/2}, \end{aligned}\tag{B2}$$

$$\begin{aligned}\sin\theta_{L/2}\partial_\tau\varphi_{L/2} &= \cos\theta_{L/2}\sin\theta_{L/2-1}\cos(\varphi_{L/2-1}-\varphi_{L/2}) \\ &\quad -\sin\theta_{L/2}\cos\theta_{L/2-1} \\ &\quad +(D/J)\cos\theta_{L/2}\sin\theta_{L/2-1}\sin(\varphi_{L/2}-\varphi_{L/2-1}) \\ &\quad +(\beta_0+\beta_s)\cos\theta_{L/2}\cos\varphi_{L/2}. \end{aligned}\tag{B3}$$

The system (9) and (10) originates from (B2) and (B3) in a continuum limit. Equation (22) for the wave vector of the ground state is obtained if we take $\varphi_i = q_s z_i$ and $\theta_i = \pi/2$. A treatment for the left edge may be done in a similar way.

APPENDIX C: GENERAL SCHEME OF THE DAVIS-PUSZKARSKI EQUATION FOR ONE-DIMENSIONAL NONCOLLINEAR MAGNETIC STRUCTURE

For convenience of applications to the standing spin wave problem in a noncollinear magnetic chain, we give a concise summary of the Davis-Puszkarski equation in a self-contained manner. The notation in this Appendix will be independent of that of the main body of the paper.

1. Equations of motion for the interior and the ends

We represent the arrangement of the spins on a chain with a linear length L using the polar coordinates, $\boldsymbol{S}(z) = S(\sin\theta\cos\varphi, \sin\theta\sin\varphi, \cos\theta)$. The interior system is described by a Lagrangian in a general form,

$$L[\theta,\varphi] = \hbar S\int_{-\frac{L}{2}}^{\frac{L}{2}}(\cos\theta-1)\partial_t\varphi\, dz - \int_{-\frac{L}{2}}^{\frac{L}{2}}\mathcal{H}[\theta,\varphi]dz, \tag{C1}$$

where the first term represents the kinetic Berry phase term. The effective Hamiltonian $\mathcal{H}[\theta,\varphi]$ describes a continuous model that contains spatial derivatives of θ and φ fields coming from the exchange interactions and nonlinear Zeeman terms such as $\sin\theta\cos\varphi$ or $\cos\theta$. Then, the coupled Euler-Lagrangian equations of motion are written down as

$$\hbar S\sin\theta\frac{\partial\theta}{\partial t} = \frac{\delta\mathcal{H}}{\delta\varphi}, \tag{C2}$$

$$\hbar S\sin\theta\frac{\partial\varphi}{\partial t} = -\frac{\delta\mathcal{H}}{\delta\theta}. \tag{C3}$$

Next we assume that the ground-state configurations $\theta_0(z)$ and $\varphi_0(z)$ are given through the stationarity condition $\delta\int\mathcal{H}[\theta,\varphi]dz = 0$, and we consider the small (Gaussian) fluctuations $\delta\theta(z,t)$ and $\delta\varphi(z,t)$,

$$\theta(z,t) = \theta_0(z) + \delta\theta(z,t), \tag{C4}$$

$$\varphi(z,t) = \varphi_0(z) + \delta\varphi(z,t). \tag{C5}$$

Expanding the EOMs (C2) and (C3), we may obtain the EOMs for the fluctuations in a general form,

$$\frac{\partial\delta\theta(z,t)}{\partial t} = \hat{\mathcal{L}}_\varphi\delta\varphi(z,t) + \epsilon f(z,t), \tag{C6}$$

$$\frac{\partial\delta\varphi(z,t)}{\partial t} = -\hat{\mathcal{L}}_\theta\delta\theta(z,t), \tag{C7}$$

where $\hat{\mathcal{L}}_\varphi$ and $\hat{\mathcal{L}}_\theta$ are linear differential operators. Without loss of generality, we introduce a small external force term $\epsilon f(z,t)$. From now on, we consider two cases: $\epsilon = 0$ and finite $\epsilon \neq 0$.

Next we address EOMs for the end spins. We start with the lattice Hamiltonian and write down the EOMs for the end spins, $\boldsymbol{S}_1$ and $\boldsymbol{S}_N$, which couple with the nearest-neighbor interior spins $\boldsymbol{S}_2$ and $\boldsymbol{S}_{N-1}$, respectively. For example, for the right-side end ($z = L/2$), the continuum limit is taken as

$$\varphi_{N-1} \sim \varphi(L/2) - a\frac{\partial\varphi(z)}{\partial z} + \frac{a^2}{2}\frac{\partial^2\varphi(z)}{\partial z^2}, \tag{C8}$$

and then evaluating the derivative at $z = L/2$. Thus, we obtain the EOMs at the ends,

$$\frac{\partial\delta\theta_s(z,t)}{\partial t} = \hat{\mathcal{M}}_\varphi\delta\varphi_s(z,t) + \epsilon f(z,t), \tag{C9}$$

$$\frac{\partial\delta\varphi_s(z,t)}{\partial t} = -\hat{\mathcal{M}}_\theta\delta\theta_s(z,t). \tag{C10}$$

Here, $\hat{\mathcal{M}}_\varphi$ and $\hat{\mathcal{M}}_\theta$ are the linear operators including the effects of the surface pinning fields. After acting with these operators on $\delta\varphi_s(z,t)$ and $\delta\theta_s(z,t)$, respectively, we fix $z = z_s = \pm L/2$, and, consequently, a dependence on the interior coordinate, z, disappears.

2. The case of $\epsilon = 0$

In the case of $\epsilon = 0$, Eqs. (C6) and (C7) are solved using a separation of variables,

$$\delta\theta(z,t) = \mu(z)M(t), \tag{C11}$$

$$\delta\varphi(z,t) = \nu(z)N(t). \tag{C12}$$

Inserting these forms into Eqs. (C6) and (C7), we obtain

$$\frac{1}{N(t)}\frac{\partial M(t)}{\partial t} = \frac{1}{\mu(z)}\hat{\mathcal{L}}_\varphi\nu(z) = C_1, \tag{C13}$$

$$\frac{1}{M(t)}\frac{\partial N(t)}{\partial t} = -\frac{1}{\nu(z)}\hat{\mathcal{L}}_\theta\mu(z) = -C_2, \tag{C14}$$

with C_1 and C_2 being constants. Then the temporal constituents immediately give the eigenfrequency for the interior system,

$$\Omega_{\text{interior}} = \sqrt{C_1C_2}. \tag{C15}$$

Next let us consider the spatial parts,

$$\hat{\mathcal{L}}_\varphi \nu(z) = C_1 \mu(z), \tag{C16}$$

$$\hat{\mathcal{L}}_\theta \mu(z) = C_2 \nu(z). \tag{C17}$$

Here we assume that the differential operators $\hat{\mathcal{L}}_\theta$ and $\hat{\mathcal{L}}_\varphi$ have simultaneous eigenfunctions, $\Psi_q(z)$, labeled by an index q. That is to say,

$$\hat{\mathcal{L}}_\theta \Psi_q(z) = \lambda_\theta(q)\Psi_q(z), \tag{C18}$$

$$\hat{\mathcal{L}}_\varphi \Psi_q(z) = \lambda_\varphi(q)\Psi_q(z). \tag{C19}$$

Expanding $\mu(z)$ and $\nu(z)$in terms of $\Psi_q(z)$ as the orthogonal basis,

$$\mu(z) = \textstyle\sum_q \mu_q \Psi_q(z), \tag{C20}$$

$$\nu(z) = \textstyle\sum_q \nu_q \Psi_q(z), \tag{C21}$$

we have

$$\textstyle\sum_q [\nu_q \lambda_\varphi(q) - C_1 \mu_q]\Psi_q(z) = 0, \tag{C22}$$

$$\textstyle\sum_q [\mu_q \lambda_\theta(q) - C_2 \nu_q]\Psi_q(z) = 0, \tag{C23}$$

which lead to

$$C_1 = \frac{\nu_q}{\mu_q}\lambda_\varphi(q),\ C_2 = \frac{\mu_q}{\nu_q}\lambda_\theta(q). \tag{C24}$$

Therefore, we can replace Eq. (C15) with

$$\Omega_{\text{interior}}(q) = \sqrt{\lambda_\theta(q)\lambda_\varphi(q)}. \tag{C25}$$

Now, let us turn attention to the fluctuations at the ends, described in a form

$$\delta\theta_{\text{s}}(t) = \delta\theta(z_{\text{s}}, t) = c_1 \Psi_q(z_{\text{s}}) M_{\text{s}}(t), \tag{C26}$$

$$\delta\varphi_{\text{s}}(t) = \delta\varphi(z_{\text{s}}, t) = c_2 \Psi_q(z_{\text{s}}) N_{\text{s}}(t), \tag{C27}$$

with c_1 and c_2 being constants, and $z_{\text{s}} = \pm L/2$. Note that the surface states "participate in" or are "swallowed up by" the interior mode specified by q. Inserting them into Eqs. (C9) and (C10), we may have

$$\frac{\partial M_{\text{s}}(t)}{\partial t} = A_q N_{\text{s}}(t), \tag{C28}$$

$$\frac{\partial N_{\text{s}}(t)}{\partial t} = -B_q M_{\text{s}}(t), \tag{C29}$$

where A_q and B_q contain spatial derivatives of $\Psi_q(z)$ at $z = z_{\text{s}}$, i.e., no linear differential operator appears. We dropped an external force term, since information on A_q and B_q is enough to obtain the Larmor frequency of the surface end spins,

$$\Omega_{\text{surface}}(q) = \sqrt{A_q B_q}. \tag{C30}$$

Now, the matching condition

$$\Omega_n \equiv \Omega_{\text{surface}}(q_n) = \Omega_{\text{interior}}(q_n) \tag{C31}$$

gives the Davis-Puszkarski equation, which determines a series of allowed values of q_n ($n = 1, 2, \dots$) corresponding to the SSW modes. In the context of this paper, this corresponds to the Pincus mode.

3. The case of $\epsilon \neq 0$

The existence of the space-time-dependent term $\epsilon f(z, t)$ prevents us from using a separation of variables. We then seek the interior solution in a perturbative manner based on an ansatz,

$$\delta\theta(z, t) = \frac{\mu(z)}{\mu_{\text{s}}}\delta\theta_{\text{s}}(t) + \epsilon\tilde{\psi}(z, t), \tag{C32}$$

$$\delta\varphi(z, t) = \frac{\nu(z)}{\nu_{\text{s}}}\delta\varphi_{\text{s}}(t) + \epsilon\tilde{\chi}(z, t), \tag{C33}$$

where μ_{s} and ν_{s} are, respectively, the values of $\mu(z)$ and $\nu(z)$ at the surface ends. In this ansatz, we implicitly assume that the time dependences at the surface, $\delta\theta_{\text{s}}(t)$ and $\delta\varphi_{\text{s}}(t)$, are known. We impose here the boundary condition,

$$\tilde{\psi}(z_{\text{s}}, t) = \tilde{\chi}(z_{\text{s}}, t) = 0, \tag{C34}$$

which means the perfect pinning of the $\tilde{\chi}$ and $\tilde{\psi}$ fields at the ends. Due to these conditions, we consistently reproduce

$$\delta\theta(z_{\text{s}}, t) = \delta\theta_{\text{s}}(t), \tag{C35}$$

$$\delta\varphi(z_{\text{s}}, t) = \delta\varphi_{\text{s}}(t) \tag{C36}$$

at the surfaces.

a. Pincus mode

Now, we proceed with analysis in a perturbative manner. Collecting the zeroth-order terms with respect to ϵ, we have

$$\frac{1}{\delta\varphi_{\text{s}}(t)}\frac{\partial\delta\theta_{\text{s}}(t)}{\partial t} = \frac{\mu_{\text{s}}}{\nu_{\text{s}}}\frac{1}{\mu(z)}\hat{\mathcal{L}}_\varphi \nu(z) = D_1, \tag{C37}$$

$$\frac{1}{\delta\theta_{\text{s}}(t)}\frac{\partial\delta\varphi_{\text{s}}(t)}{\partial t} = -\frac{\nu_{\text{s}}}{\mu_{\text{s}}}\frac{1}{\nu(z)}\hat{\mathcal{L}}_\theta \mu(z) = -D_2, \tag{C38}$$

with D_1 and D_2 being constants. Then, as in the case of $\epsilon = 0$, the eigenfrequency for the interior system is given by

$$\Omega_{\text{interior}}(q) = \sqrt{D_1 D_2} = \sqrt{\lambda_\varphi(q)\lambda_\theta(q)}. \tag{C39}$$

Let us then turn attention to the surface spins. In the vicinity of the ends, $\tilde{\psi}(z, t)$ and $\tilde{\chi}(z, t)$ can be dropped and we have

$$\delta\theta(z, t) = c_1 \Psi_q(z)\delta\theta_{\text{s}}(t). \tag{C40}$$

$$\delta\varphi(z, t) = c_2 \Psi_q(z)\delta\varphi_{\text{s}}(t), \tag{C41}$$

with c_1 and c_2 being constants. It should be noted that the basis function $\Psi_q(z)$ is now specified just as in the case of (C26) and (C27). Inserting them into Eqs. (C9) and (C10), we obtain the zeroth-order equations,

$$\frac{\partial\delta\theta_{\text{s}}(t)}{\partial t} = \frac{c_2}{c_1}F_q \delta\varphi_{\text{s}}(t), \tag{C42}$$

$$\frac{\partial\delta\varphi_{\text{s}}(t)}{\partial t} = -\frac{c_1}{c_2}G_q \delta\theta_{\text{s}}(t), \tag{C43}$$

where F_q and G_q contain spatial derivatives of $\Psi_q(z)$ at $z = z_{\text{s}}$. We thus obtain the Larmor frequency of the surface end spins,

$$\Omega_{\text{surface}}(q) = \sqrt{F_q G_q}. \tag{C44}$$

Now, the matching condition

$$\Omega_n \equiv \Omega_{\text{surface}}(q_n) = \Omega_{\text{interior}}(q_n) \tag{C45}$$

again gives the Davis-Puszkarski equation. In the context of this paper, this corresponds to the Pincus mode.

b. Kittel ripple

Next, we consider the first-order terms to obtain

$$\frac{\partial\tilde{\psi}(z,t)}{\partial t} = \hat{\mathcal{L}}_{\varphi}\tilde{\chi}(z,t) + f(z,t), \tag{C46}$$

$$\frac{\partial\tilde{\chi}(z,t)}{\partial t} = -\hat{\mathcal{L}}_{\theta}\tilde{\psi}(z,t), \tag{C47}$$

where the linear operators, $\hat{\mathcal{L}}_{\varphi}$ and $\hat{\mathcal{L}}_{\theta}$, for the interior system appear. Again, we expand $\tilde{\psi}(z,t)$ and $\tilde{\chi}(z,t)$in terms of $\Psi_Q(z)$,

$$\tilde{\psi}(z,t) = \textstyle\sum_Q \tilde{\psi}_Q(t)\Psi_Q(z), \tag{C48}$$

$$\tilde{\chi}(z,t) = \textstyle\sum_Q \tilde{\chi}_Q(t)\Psi_Q(z). \tag{C49}$$

In this case, *the allowed Q is determined solely by the perfect pinning condition*

$$\Psi_{Q_n}(z_s) = 0. \tag{C50}$$

We should note the essential difference between the conditions (C45) and (C50).

We insert Eqs. (C48) and (C49) into Eqs. (C46) and (C47), take one more time derivative, multiply both sides by $\Psi_Q(z)$, and integrate over z to obtain

$$\frac{d^2\tilde{\psi}_Q(t)}{dt^2} = -\lambda_\theta(Q)\lambda_\varphi(Q)\tilde{\psi}_Q(t) + \frac{df_Q(t)}{dt}, \tag{C51}$$

$$\frac{d^2\tilde{\chi}_Q(t)}{dt^2} = -\lambda_\varphi(Q)\lambda_\theta(Q)\tilde{\chi}_Q(t) - \lambda_\theta(Q)f_Q(t), \tag{C52}$$

where

$$f_Q(t) = \frac{\int_{-L/2}^{L/2}\Psi_Q(z)f(z,t)dz}{\int_{-L/2}^{L/2}\Psi_Q^2(z)dz}. \tag{C53}$$

Now the eigenfrequency,

$$\tilde{\Omega}_n = \sqrt{\lambda_\theta(Q_n)\lambda_\varphi(Q_n)}, \tag{C54}$$

specifies the modes associates with $\tilde{\psi}(z,t)$ and $\tilde{\chi}(z,t)$, i.e., the Kittel ripple in the present context. Equations (C51) and (C52) are readily solved to give

$$\tilde{\psi}_{Q_n}(t) = \frac{1}{\tilde{\Omega}_n}\int_0^t \frac{df_Q(t')}{dt'}\sin[\tilde{\Omega}_n(t-t')]dt', \tag{C55}$$

$$\tilde{\chi}_{Q_n}(t) = -\frac{\tilde{\lambda}_\theta(Q)}{\tilde{\Omega}_n}\int_0^t f_Q(t')\sin[\tilde{\Omega}_n(t-t')]dt', \tag{C56}$$

provided $f_Q(0) = 0$. Finally, we note

$$\Omega_n < \tilde{\Omega}_n, \tag{C57}$$

because the Kittel modes, $\tilde{\psi}(z,t)$ and $\tilde{\chi}(z,t)$, are strictly confined into the system over the region $-L/2 \leqslant z \leqslant L/2$. On the other hand, the Pincus mode can be extended beyond this region. This makes Ω_n smaller than $\tilde{\Omega}_n$ for a common n.

[1] A. Barman and J. Sinha, *Spin Dynamics and Damping in Ferromagnetic Thin Films and Nanostructures* (Springer, Cham, Switzerland, 2018).

[2] Y. Togawa, T. Koyama, K. Takayanagi, S. Mori, Y. Kousaka, J. Akimitsu, S. Nishihara, K. Inoue, A. S. Ovchinnikov, and J. Kishine, Phys. Rev. Lett. **108**, 107202 (2012).

[3] Y. Togawa, Y. Kousaka, S. Nishihara, K. Inoue, J. Akimitsu, A. S. Ovchinnikov, and J. Kishine, Phys. Rev. Lett. **111**, 197204 (2013).

[4] L. Wang, N. Chepiga, D.-K. Ki, L. Li, F. Li, W. Zhu, Y. Kato, O. S. Ovchinnikova, F. Mila, I. Martin, D. Mandrus, and A. F. Morpurgo, Phys. Rev. Lett. **118**, 257203 (2017).

[5] Y. Togawa, T. Koyama, Y. Nishimori, Y. Matsumoto, S. McVitie, D. McGrouther, R. L. Stamps, Y. Kousaka, J. Akimitsu, S. Nishihara, K. Inoue, I. G. Bostrem, Vl. E. Sinitsyn, A. S. Ovchinnikov, and J. Kishine, Phys. Rev. B **92**, 220412(R) (2015).

[6] J. Kishine and A. S. Ovchinnikov, Solid State Phys. **66**, 1 (2015).

[7] J.-i. Kishine, I. Proskurin, I. G. Bostrem, A. S. Ovchinnikov, and Vl. E. Sinitsyn, Phys. Rev. B **93**, 054403 (2016).

[8] J.-i. Kishine and A. S. Ovchinnikov, Phys. Rev. B **79**, 220405(R) (2009).

[9] V. V. Kiselev and A. A. Raskovalov, J. Exp. Theor. Phys. **116**, 272 (2013).

[10] F. J. T. Goncalves, T. Sogo, Y. Shimamoto, Y. Kousaka, J. Akimitsu, S. Nishihara, K. Inoue, D. Yoshizawa, M. Hagiwara, M. Mito, R. L. Stamps, I. G. Bostrem, V. E. Sinitsyn, A. S. Ovchinnikov, J. Kishine, and Y. Togawa, Phys. Rev. B **95**, 104415 (2017).

[11] F. J. T. Goncalves, T. Sogo, Y. Shimamoto, I. Proskurin, Vl. E. Sinitsyn, Y. Kousaka, I. G. Bostrem, J. Kishine, A. S. Ovchinnikov, and Y. Togawa, Phys. Rev. B **98**, 144407 (2018).

[12] C. Kittel, Phys. Rev. **110**, 1295 (1958).

[13] P. Pincus, Phys. Rev. **118**, 658 (1960).

[14] J. R. Davis and F. Keffer, J. Appl. Phys. **34**, 1135 (1963).

[15] H. Puszkarski, IEEE Trans. Magn. **9**, 22 (1973).

[16] J. R. Banavar and F. Keffer, Phys. Rev. B **17**, 2974 (1978).

[17] M. H. Seavey, Jr. and P. E. Tannenwald, Phys. Rev. Lett. **1**, 168 (1958).

[18] S. E. Lofland, S. M. Bhagat, C. Kwon, M. C. Robson, R. P. Sharma, R. Ramesh, and T. Venkatesan, Phys. Lett. A **209**, 246 (1995).

[19] M. Mruczkiewicz, M. Krawczyk, V. K. Sakharov, Yu. V. Khivintsev, Yu. A. Filimonov, and S. A. Nikitov, J. Appl. Phys. **113**, 093908 (2013).
[20] M. P. Wismayer, B. W. Southern, X. L. Fan, Y. S. Gui, C.-M. Hu, and R. E. Camley, Phys. Rev. B **85**, 064411 (2012).
[21] P. Buczek, A. Ernst, and L. M. Sandratskii, Phys. Rev. Lett. **105**, 097205 (2010).
[22] A. A. Serga, A. V. Chumak, A. Andre, G. A. Melkov, A. N. Slavin, S. O. Demokritov, and B. Hillebrands, Phys. Rev. Lett. **99**, 227202 (2007).
[23] A. V. Chumak, A. A. Serga, B. Hillebrands, G. A. Melkov, V. Tiberkevich, and A. N. Slavin, Phys. Rev. B **79**, 014405 (2009).
[24] S. Klingler, V. Amin, S. Geprägs, K. Ganzhorn, H. Maier-Flaig, M. Althammer, H. Huebl, R. Gross, R. D. McMichael, M. D. Stiles, S. T. B. Goennenwein, and M. Weiler, Phys. Rev. Lett. **120**, 127201 (2018).
[25] R. Magaraggia, K. Kennewell, M. Kostylev, R. L. Stamps, M. Ali, D. Greig, B. J. Hickey, and C. H. Marrows, Phys. Rev. B **83**, 054405 (2011).
[26] J.-i. Kishine, I. G. Bostrem, A. S. Ovchinnikov, and Vl. E. Sinitsyn, Phys. Rev. B **89**, 014419 (2014).
[27] M. N. Wilson, E. A. Karhu, D. P. Lake, A. S. Quigley, S. Meynell, A. N. Bogdanov, H. Fritzsche, U. K. Rößler, and T. L. Monchesky, Phys. Rev. B **88**, 214420 (2013).
[28] R. F. Soohoo, Phys. Rev. **131**, 594 (1963).
[29] G. Rado and J. Weertman, J. Phys. Chem. Solids **11**, 315 (1959).
[30] M. Sparks, Phys. Rev. B **1**, 3831 (1970).
[31] M. W. Gutowski, arXiv:1312.7130.
[32] M. Shinozaki1, S. Hoshino, Y. Masaki, J. Kishine, and Y. Kato, J. Phys. Soc. Jpn. **85**, 074710 (2016).
[33] I. E. Dzyaloshinskii, Zh. Eksp. Teor. Fiz. **46**, 1420 (1964) [Sov. Phys. JETP **19**, 960 (1964)]; Zh. Eksp. Teor. Fiz. **47**, 992 (1964) [Sov. Phys. JETP **20**, 665 (1965)].
[34] Yu. A. Izyumov, Sov. Phys. Usp. **27**, 845 (1984).
[35] J.-i. Kishine, I. G. Bostrem, A. S. Ovchinnikov, and V. E. Sinitsyn, Phys. Rev. B **86**, 214426 (2012).
[36] B. Sutherland, Phys. Rev. A **8**, 2514 (1973).
[37] Yu. A. Izyumov, *Difrakciya Neytronov na Dlinnoperiodicheskih Structurah* (Neutron diffraction on long-peiodic structures) (Energoatomizdat, Moscow, 1987) (in Russian), see p. 126 therein.
[38] We use Kittel's terminology here, where the SSW order corresponds to a number of half-wavelengths on a line.
[39] T. Miyadai, K. Kikuchi, H. Kondo, S. Sakka, M. Arai, and Y. Ishikawa, Phys. Soc. Jpn. **52**, 1394 (1983).
[40] A. Polyanin, *Handbook of Linear Partial Differential Equations for Engineers and Scientists* (Chapman Hall/CRC, Boca Raton, FL, 2002), Sec. 0.11.1 therein.
[41] S. A. Meynell, M. N. Wilson, H. Fritzsche, A. N. Bogdanov, and T. L. Monchesky, Phys. Rev. B **90**, 014406 (2014).
[42] A. I. Akhiezer, V. G. Baryakhtar, and S. V. Peletminskii, *Spin Waves* (North Holland, Amsterdam, 1968), See Eq. (5.5.10) therein.
[43] R. W. Damon and J. R. Eshbach, J. Phys. Chem. Solids **19**, 308 (1961).
[44] M. J. Hurben and C. E. Patton, J. Magn. Magn. Mater. **139**, 263 (1995).
[45] R. E. Arias, Phys. Rev. B **94**, 134408 (2016).
[46] A. T. Costa, R. B. Muniz, and D. L. Mills, Phys. Rev. B **69**, 064413 (2004).
[47] J. M. Lock, Br. J. Appl. Phys. **17**, 1645 (1966).
[48] M. A. W. Schoen, J. M. Shaw, H. T. Nembach, M. Weiler, and T. J. Silva, Phys. Rev. B **92**, 184417 (2015).
[49] Y. Li and W. E. Bailey, Phys. Rev. Lett. **116**, 117602 (2016).